β decay of deformed r-process nuclei near $A = 80$ and $A = 160$, including odd-A and odd-odd nuclei, with the Skyrme finite-amplitude method

T. Shafer* and J. Engel†
Department of Physics and Astronomy, CB 3255, University of North Carolina, Chapel Hill, North Carolina 27599-3255

C. Fröhlich and G. C. McLaughlin
Department of Physics, North Carolina State University, Box 8202, Raleigh, North Carolina 27695

M. Mumpower
Department of Physics, University of Notre Dame, Notre Dame, Indiana 46556
and Theory Division, Los Alamos National Laboratory, Los Alamos, New Mexico 87544

R. Surman
Department of Physics, University of Notre Dame, Notre Dame, Indiana 46556
(Received 22 June 2016; revised manuscript received 3 September 2016; published 7 November 2016)

After identifying the nuclei in the $A \simeq 80$ and $A \simeq 160$ regions for which β-decay rates have the greatest effect on weak and main r-process abundance patterns, we apply the finite-amplitude method (FAM) with Skyrme energy-density functionals (EDFs) to calculate β-decay half-lives of those nuclei in the quasiparticle random-phase approximation (QRPA). We use the equal filling approximation to extend our implementation of the charge-changing FAM, which incorporates pairing correlations and allows axially symmetric deformation, to odd-A and odd-odd nuclei. Repeated calculations with $A \simeq 160$ nuclei and multiple EDFs show a spread of 1.9–3.3 in β-decay half-lives, with differences in calculated Q values playing an important role. We compare our results with those of previous work and investigate their implications for r-process simulations.

DOI: 10.1103/PhysRevC.94.055802

I. INTRODUCTION

The solar abundances of nuclei heavier than iron, on the neutron-rich side of stability, have traditionally been attributed to rapid neutron-capture, or r-process, nucleosynthesis [1]. The three largest abundance peaks in the solar pattern, at $A \sim 80$, 130, and 195, are associated with the closed neutron shells at $N = 50$, 82, and 126, suggesting that astrophysical conditions of increasing neutron richness are responsible for each. A smaller fourth abundance peak in the rare-earth elements ($A \sim 160$) is also formed in neutron-rich environments. Observational data from meteorites and metal-poor halo stars confirm the separate origins for $70 \lesssim A \lesssim 120$ ("weak") and $A > 120$ ("main") r-process nuclei and provide hints of the nature of the r-process astrophysical site, though the exact site (or sites) has not yet been definitively pinned down [2].

In principle the r-process sites can be identified by comparing simulations of prospective astrophysical environments with observational data from the solar system and other stars (see, e.g., Ref. [3]). The precision of r-process abundance predictions, however, is limited by our incomplete knowledge of properties—such as masses, reaction rates, and decay lifetimes—of nuclei on the neutron-rich side of stability [4]. It is particularly important that we better determine decay lifetimes, because r-process nuclei are built up via a sequence of captures and β decays. Thus, β-decay lifetimes determine the relative abundances of the nuclei along the r-process path [1,2,5] and the overall time scale for neutron capture [6,7]. At late times, as nuclei move back from the r-process path toward stability and the last remaining neutrons are captured, the lifetimes determine the shape of the final abundance pattern [5,8]. Finally, for a weak r process β-decay rates control the amount of material that remains trapped in the $A \sim 80$ peak and the amount that moves to higher mass numbers [9], i.e., they determine where the weak r process terminates. For all these reasons, an accurate picture of the β decay of neutron-rich nuclei is crucial for the accuracy of r-process simulations.

Although many β-decay lifetimes have been measured (see, e.g., Refs. [9–13]), most of the nuclei populated during the r process remain out of reach. Simulations must therefore rely on calculated lifetimes. The most widely used sets of theoretical rates are from gross theory [14–16] and from an application of the quasiparticle random-phase approximation (QRPA) within a macroscopic-microscopic framework [6,17] that employs gross theory for first-forbidden transitions. Here we use a fully microscopic Skyrme QRPA, implemented through the proton-neutron finite-amplitude method (pnFAM) [18] and extended to treat odd-A and odd-odd nuclei (hereafter "odd" nuclei) in the equal-filling approximation (EFA) [19]. We can now use arbitrary Skyrme energy-density functionals (EDFs) to self-consistently compute β-decay rates of both even-even and odd axially symmetric nuclei, including contributions of both allowed ($J^\pi = 1^+$) and first-forbidden ($J^\pi = 0^-, 1^-$, or 2^-) transitions.

*tom@tshafer.com
†engelj@physics.unc.edu

We evaluate lifetimes for key r-process nuclei in two highly populated regions of the abundance pattern: the large maximum at $A \sim 80$ and the smaller rare-earth peak at $A \sim 160$. In a main r process, the rare earth peak forms in a different way than do the large peaks at $A \sim 130$ and 195, both of which originate from long-lived "waiting points" near closed neutron shells at $N = 82$ and 126. The rare-earth peak, by contrast, forms during the late stages of the r process, as β decay, neutron capture, and photodissociation all compete with one another and the r-process path moves toward stability [20,21]. The $A \sim 160$ abundance peak is thus useful for studying the main r-process environment [22,23]. The $A \sim 80$ region is not so clearly related to the main r process. In fact, nuclei with $70 \lesssim A \lesssim 120$ can be created in a variety of nucleosynthetic processes, ranging from the neutron-rich weak r process to the proton-rich νp process [24–26] (see also Refs. [27,28]). Untangling the various contributions to these elements requires rigorous abundance pattern predictions, which in turn require a better knowledge of still unmeasured β-decay half-lives.

In this paper, we aim to study and improve r-process abundance predictions for both weak r-process nuclei and the rare-earth elements by identifying and recalculating key β-decay rates. We begin in Sec. II by reviewing the pnFAM and then discussing our extension to odd nuclei. In Sec. III, guided by r-process sensitivity studies, we calculate β-decay rates separately for the important isotopes in the two mass regions (after optimizing the Skyrme EDF separately for each region). We also examine the effect on β-decay half-lives of varying the Skyrme EDF in rare-earth nuclei. Finally, in Sec. IV we discuss the impact of our β-decay rates on r-process abundances. Section V is a conclusion.

II. NUCLEAR STRUCTURE

A. The proton-neutron finite-amplitude method

The finite-amplitude method (FAM) is an efficient way to calculate strength distributions in the random-phase approximation (RPA) or the QRPA. Nakatsukasa *et al.* first introduced the FAM to calculate the RPA response of deformed nuclei [29] with Skyrme EDFs, and the method was rapidly extended to include pairing correlations in Skyrme QRPA, both for spherical [30] and axially deformed nuclei [31], and to include similar correlations in the relativistic QRPA [32]. Reference [18] applied the same ideas to charge-changing transitions, in particular those involved in β decay; the resulting method is called the pnFAM. Like the FAM implemented in Ref. [31], the pnFAM computes strength functions for transitions that change the K quantum number by arbitrary (integer) amounts in spherical or deformed superfluid nuclei.

The first work with the pnFAM focused on the impact of tensor terms in Skyrme EDFs [18]. More recently, the authors of Ref. [33] used the method to constrain the time-odd part of the Skyrme EDF and compute a β-decay table that includes the half-lives of 1387 even-even nuclei. We leave most details of the pnFAM itself to these references, but repeat the main points here in anticipation of the extension to odd nuclei in Sec. II B.

QRPA strength functions are related to the linear time-dependent response of the Hartree-Fock-Bogoliubov (HFB) mean field (see, e.g., Refs. [34,35] for a discussion). The static HFB equation can be written as

$$[\mathcal{H}_0, \mathcal{R}_0] = 0, \tag{1}$$

where (e.g., for protons or neutrons)

$$\mathcal{R}_0 = \begin{pmatrix} \rho_0 & \kappa_0 \\ -\kappa_0^* & 1-\rho_0^* \end{pmatrix}, \quad \mathcal{H}_0 = \begin{pmatrix} h_0 & \Delta_0 \\ -\Delta_0^* & -h_0^* \end{pmatrix}. \tag{2}$$

In Eq. (2), $\mathcal{R}_0$ is the generalized static density (the subscript 0 indicates a static quantity), built from the single-particle density ρ_0 and the pairing tensor κ_0 (see, e.g., Ref. [34]), and $\mathcal{H}_0$ is the static generalized mean field, built from the static mean field h_0 and the static pairing field Δ_0. The generalized mean field $\mathcal{H}_0$ depends on both ρ_0 and κ_0 and is usually written $\mathcal{H}_0[\mathcal{R}_0]$. The matrices $\mathcal{R}_0$ and $\mathcal{H}_0$ are diagonalized by a unitary Bogoliubov transformation,

$$\mathbb{W} = \begin{pmatrix} U & V^* \\ V & U^* \end{pmatrix}, \tag{3}$$

which connects the set of single-particle states (created by $c_k^\dagger$) in which the problem is formulated to a set of quasiparticle states (created by $\alpha_\mu^\dagger$):

$$\begin{pmatrix} c \\ c^\dagger \end{pmatrix} = \begin{pmatrix} U & V^* \\ V & U^* \end{pmatrix} \begin{pmatrix} \alpha \\ \alpha^\dagger \end{pmatrix}. \tag{4}$$

Thus, the transformed generalized density and mean field,

$$\mathbb{R}_0 \equiv \mathbb{W}^\dagger \mathcal{R}_0 \mathbb{W}, \quad \mathbb{H}_0 \equiv \mathbb{W}^\dagger \mathcal{H}_0 \mathbb{W}, \tag{5}$$

are in the quasiparticle basis and have the diagonal form,

$$\mathbb{R}_0 = \begin{pmatrix} 0 & 0 \\ 0 & 1 \end{pmatrix}, \quad \mathbb{H}_0 = \begin{pmatrix} E & 0 \\ 0 & -E \end{pmatrix}. \tag{6}$$

In the pnFAM we solve the small-amplitude time-dependent HFB (TDHFB) equation,

$$i\dot{\mathbb{R}}(t) = [\mathbb{H}[\mathbb{R}(t)] + \mathbb{F}(t), \mathbb{R}(t)], \tag{7}$$

where $\mathbb{F}(t)$ is a time-dependent external field that changes neutrons into protons or vice versa. Equation (7) determines the oscillation of the generalized density around the static solution $\mathbb{R}_0$ of Eq. (1); for external fields proportional to a small parameter η, a first-order expansion $\mathbb{R}(t) \approx \mathbb{R}_0 + \eta\delta\mathbb{R}(t)$ is sufficient to describe the behavior of the nucleus. It leads to the linear-response equation:

$$i\delta\dot{\mathbb{R}}(t) = [\mathbb{H}_0, \delta\mathbb{R}(t)] + [\delta\mathbb{H}(t) + \mathbb{F}(t), \mathbb{R}_0]. \tag{8}$$

Here $\delta\mathbb{H}(t)$ and $\delta\mathbb{R}(t)$ are the first-order changes in the generalized mean field and density.

If the perturbing field oscillates at a frequency ω, the resulting generalized density can be written in the form:

$$\delta\mathbb{R}(t) = \delta\mathbb{R}(\omega)e^{-i\omega t} + \delta\mathbb{R}^\dagger(\omega)e^{i\omega t}, \tag{9}$$

with

$$\delta\mathbb{R}(\omega) \equiv \begin{pmatrix} 0 & X(\omega) \\ -Y(\omega) & 0 \end{pmatrix}, \tag{10}$$

where the requirement that $\mathbb{R}(t)$ remain projective ($\mathbb{R}^2 = \mathbb{R}$) forces the diagonal blocks to be zero [32]. The time-dependent generalized Hamiltonian also oscillates harmonically, with

$$\delta\mathbb{H}(\omega) = \begin{pmatrix} \delta H^{11}(\omega) & \delta H^{20}(\omega) \\ -\delta H^{02}(\omega) & -\delta H^{\overline{11}}(\omega) \end{pmatrix}. \tag{11}$$

The block superscripts refer to the number of quasiparticles created and destroyed by the corresponding block Hamiltonian (cf. Refs. [30,32]); the 20 and 02 blocks are made up of terms proportional to $\alpha^\dagger\alpha^\dagger$ and $\alpha\alpha$, respectively, and the 11 and $\overline{11}$ blocks of terms proportional to $\alpha^\dagger\alpha$ and $\alpha\alpha^\dagger$.

Putting everything together in Eq. (8) [including the oscillating external field $\mathbb{F}(t)$, which we have not written out explicitly here], and evaluating the commutators, one obtains the pnFAM equations [18]:

$$X_{\pi\nu}(E_\pi + E_\nu - \omega) + \delta H^{20}_{\pi\nu}(\omega) = -F^{20}_{\pi\nu}, \tag{12a}$$

$$Y_{\pi\nu}(E_\pi + E_\nu + \omega) + \delta H^{02}_{\pi\nu}(\omega) = -F^{02}_{\pi\nu}, \tag{12b}$$

where π and ν label proton and neutron states, and E_π and E_ν are single-quasiparticle energies. Equation (12) can be put into matrix-QRPA form [30], but it is more easily solved directly (through iteration) [18,29,30]. The FAM transition strength is then just given by $S(F;\omega) = \mathrm{tr}\,\mathbb{F}^\dagger\delta\mathbb{R}^{(pn)}(\omega)$ [18,29,30].

B. The equal-filling approximation and the linear response of odd nuclei

Our pnFAM code and HFBTHO, the HFB code on which it is based, require time-reversal-symmetric nuclear states [36]. To apply the FAM to odd nuclei, the ground states of which break time-reversal symmetry, we use the EFA, a "phenomenological" approximation, in the words of Ref. [19], in which the interaction between the odd nucleon and the core are captured at least partially without breaking time-reversal symmetry.

In odd-nucleus density-functional theory, the ground state is typically represented in leading order by a one-quasiparticle excitation of an even-even core, $|\Phi_\Lambda\rangle = \alpha^\dagger_\Lambda|\Phi\rangle$. This state, however, produces the time-reversal-breaking single-particle and pairing densities [19,37],

$$\rho_{kk'} = (V^*V^T)_{kk'} + U_{k\Lambda}U^*_{k'\Lambda} - V^*_{k\Lambda}V_{k'\Lambda}, \tag{13a}$$

$$\kappa_{kk'} = (V^*U^T)_{kk'} + U_{k\Lambda}V^*_{k'\Lambda} - V^*_{k\Lambda}U_{k'\Lambda}. \tag{13b}$$

The EFA replaces the densities in Eq. (13) with new ones that average contributions from the state $\alpha^\dagger_\Lambda|\Phi\rangle$ and its time-reversed partner $\alpha^\dagger_{\bar\Lambda}|\Phi\rangle$:

$$\rho^{\mathrm{EFA}}_{kk'} = (V^*V^T)_{kk'} + \tfrac{1}{2}(U_{k\Lambda}U^*_{k'\Lambda} + U_{k\bar\Lambda}U^*_{k'\bar\Lambda} - V^*_{k\Lambda}V_{k'\Lambda} - V^*_{k\bar\Lambda}V_{k'\bar\Lambda}), \tag{14a}$$

$$\kappa^{\mathrm{EFA}}_{kk'} = (V^*U^T)_{kk'} + \tfrac{1}{2}(U_{k\Lambda}V^*_{k'\Lambda} + U_{k\bar\Lambda}V^*_{k'\bar\Lambda} - V^*_{k\Lambda}U_{k'\Lambda} - V^*_{k\bar\Lambda}U_{k'\bar\Lambda}). \tag{14b}$$

Here we have assumed that the state of the even-even core $|\Phi\rangle$ is time-reversal even. The odd-A HFB calculation then proceeds as usual with $\rho \to \rho^{\mathrm{EFA}}$ and $\kappa \to \kappa^{\mathrm{EFA}}$ [19].

The EFA appears to be an excellent approximation to the full HFB solution for odd-A nuclei. Reference [37] contains calculations of odd-proton excitation energies in rare-earth nuclei, in both the EFA and the less restrictive blocking approximation. The EFA reproduces the full one-quasiparticle energies to within a few hundred keV. The approximation was given a theoretical foundation in Ref. [19], which showed that ρ^{EFA} and κ^{EFA} can be obtained rigorously by abandoning the usual product form of the HFB solution and instead describing the nucleus as a mixed state. From this point of view, the nucleus is not represented by a single state vector $|\Phi_\Lambda\rangle$ but rather by a statistical ensemble with a density operator $\hat{\mathcal{D}} \equiv \exp\hat{K}$ [38]:

$$\hat{\mathcal{D}} = |\Phi\rangle\langle\Phi| + \sum_\mu \alpha^\dagger_\mu|\Phi\rangle p_\mu\langle\Phi|\alpha_\mu + \frac{1}{2!}\sum_{\mu\nu}\alpha^\dagger_\mu\alpha^\dagger_\nu|\Phi\rangle p_\mu p_\nu\langle\Phi|\alpha_\nu\alpha_\mu + \cdots. \tag{15}$$

In Eq. (15), p_μ is the probability that the excitation $\alpha^\dagger_\mu|\Phi\rangle$ is contained in the ensemble. Expectation values are traces with $\hat{\mathcal{D}}$ in Fock space (we use 'Tr' for these traces and 'tr' for the usual trace of a matrix),

$$\langle A\rangle = \mathrm{Tr}[\hat{\mathcal{D}}\hat{A}]/\,\mathrm{Tr}[\hat{\mathcal{D}}], \tag{16}$$

so that, e.g., the particle density is

$$\rho_{kk'} = \mathrm{Tr}[\hat{\mathcal{D}}c^\dagger_{k'}c_k]/\,\mathrm{Tr}[\hat{\mathcal{D}}]. \tag{17}$$

An ensemble like the above is familiar from finite-temperature HFB [39], where the quasiparticle occupations are statistical and determined during the HFB minimization. Reference [19] shows that the EFA emerges from a specific nonthermal choice of the ensemble probabilities:

$$p_\mu = \begin{cases} 1, & \mu \in [\Lambda, \bar\Lambda] \\ 0, & \text{otherwise.} \end{cases} \tag{18}$$

With these values of p_μ, one finds that for an arbitrary one-body operator $\hat O$,

$$\langle\hat O\rangle_{\text{o-e}} = \tfrac{1}{2}(\langle\Phi|\alpha_\Lambda\hat O\alpha^\dagger_\Lambda|\Phi\rangle + \langle\Phi|\alpha_{\bar\Lambda}\hat O\alpha^\dagger_{\bar\Lambda}|\Phi\rangle), \tag{19}$$

and the trace in Eq. (17) produces ρ^{EFA} (14a). The formalism may be applied in a straightforward way to odd-odd nuclei as well by constructing an ensemble from the proton (π) and neutron (ν) orbitals $\Lambda_\pi, \bar\Lambda_\pi, \Lambda_\nu$, and $\bar\Lambda_\nu$. Then one finds that

$$\langle\hat O\rangle_{\text{o-o}} = \tfrac{1}{2}(\langle\Phi|\alpha_{\Lambda_\nu}\alpha_{\Lambda_\pi}\hat O\alpha^\dagger_{\Lambda_\pi}\alpha^\dagger_{\Lambda_\nu}|\Phi\rangle + \langle\Phi|\alpha_{\bar\Lambda_\nu}\alpha_{\bar\Lambda_\pi}\hat O\alpha^\dagger_{\bar\Lambda_\pi}\alpha^\dagger_{\bar\Lambda_\nu}|\Phi\rangle). \tag{20}$$

The statistical interpretation of the EFA allows us to extend the pnFAM, which is an approximate time-dependent HFB, to odd nuclei. The thermal QRPA, described in Refs. [40–44], generalizes Eq. (8) to a statistical density operator $\hat{\mathcal{D}} = \exp\hat K$ and a thermal ensemble; here we do the same with the nonthermal ensemble in Eq. (18).

Of the matrices that enter the TDHFB equations (7), only the generalized density $\mathbb{R}$ is fundamentally altered in the EFA; the external field is unaffected and the ground-state Hamiltonian matrix $\mathbb{H}_0$ assumes its usual form [19]. But the

replacement $\langle\Phi|\hat{A}|\Phi\rangle$ by $\mathrm{Tr}[\hat{\mathcal{D}}\hat{A}]/\mathrm{Tr}[\hat{\mathcal{D}}]$ has implications for both the static density $\mathbb{R}_0$ and the time-dependent perturbation $\delta\mathbb{R}(t)$. In the usual HFB, the definition of the generalized density in the quasiparticle basis [34,35],

$$\mathbb{R} = \begin{pmatrix} \langle\alpha^\dagger\alpha\rangle & \langle\alpha\alpha\rangle \\ \langle\alpha^\dagger\alpha^\dagger\rangle & \langle\alpha\alpha^\dagger\rangle \end{pmatrix}, \tag{21}$$

leads to the form of $\mathbb{R}_0$ in Eq. (6). In the EFA ensemble, however, the expectation values $\langle\alpha^\dagger\alpha\rangle$ and $\langle\alpha\alpha^\dagger\rangle$ are [19]

$$\langle\alpha^\dagger_\nu\alpha_\mu\rangle = \delta_{\mu\nu} f_\mu, \tag{22a}$$

$$\langle\alpha_\nu\alpha^\dagger_\mu\rangle = \delta_{\mu\nu}(1 - f_\mu), \tag{22b}$$

leading to an $\mathbb{R}_0$ with the more general form,

$$\mathbb{R}_0^{\mathrm{EFA}} = \begin{pmatrix} f & 0 \\ 0 & 1-f \end{pmatrix}. \tag{23}$$

The matrix f is diagonal, with factors f_μ related to the p_μ (18) and taking on the values,

$$f_\mu = \begin{cases} \frac{1}{2}, & \mu \in [\Lambda, \bar{\Lambda}], \\ 0, & \text{otherwise.} \end{cases} \tag{24}$$

The use of an ensemble also changes the way we calculate the response $\delta\mathbb{R}(t)$. Following Ref. [40], we consider the evolution of the density operator under a unitary transformation $U(t) = \exp[i\eta\hat{S}(t)]$. The operator $\hat{S}(t)$ is undetermined, but Hermitian. To first order in η, the ensemble evolves as

$$\begin{aligned} \hat{\mathcal{D}}(t) &\simeq [1 + i\eta\hat{S}(t)]\hat{\mathcal{D}}(0)[1 - i\eta\hat{S}(t)] \\ &\equiv \hat{\mathcal{D}}(0) + \eta\delta\hat{\mathcal{D}}(t), \end{aligned} \tag{25}$$

with $\delta\hat{\mathcal{D}}(t) = -i[\hat{\mathcal{D}}, \hat{S}(t)]$. The cyclic invariance of the trace [19] guarantees that $\mathrm{Tr}[\delta\hat{\mathcal{D}}(t)] = 0$. The time evolution of $\hat{\mathcal{D}}(t)$ determines the evolution of $\delta\mathbb{R}(t)$, e.g., via

$$\begin{aligned} \langle\alpha^\dagger\alpha\rangle \to\ & \mathrm{Tr}[\hat{\mathcal{D}}(t)\alpha^\dagger\alpha]/\mathrm{Tr}[\hat{\mathcal{D}}(0)] \\ =\ & \langle\alpha^\dagger\alpha\rangle - i\eta\langle[\hat{S}(t), \alpha^\dagger\alpha]\rangle, \end{aligned} \tag{26}$$

so that $\delta\mathbb{R}$ is no longer block antidiagonal as in Eq. (10). Instead it has the form,

$$\delta\mathbb{R}(t) \equiv \begin{pmatrix} P_{\pi\nu}(t) & X_{\pi\nu}(t) \\ -X^*_{\pi\nu}(t) & -P^*_{\pi\nu}(t) \end{pmatrix}, \tag{27}$$

with $P(t)$ and $X(t)$ proportional to matrix elements of $\hat{S}(t)$:

$$P_{\pi\nu}(t) \equiv i(f_\nu - f_\pi)S^{11}_{\pi\nu}(t), \tag{28a}$$

$$X_{\pi\nu}(t) \equiv i(1 - f_\nu - f_\pi)S^{20}_{\pi\nu}(t). \tag{28b}$$

[The matrices S^{11} and S^{20} arise from the quasiparticle representation of the one-body operator $\hat{S}(t)$; see, e.g., the Appendix of Ref. [34].] When the external field is sinusoidal, we have

$$P_{\pi\nu}(t) = P_{\pi\nu}(\omega)e^{-i\omega t} + Q^*_{\pi\nu}(\omega)e^{i\omega t}, \tag{29a}$$

$$X_{\pi\nu}(t) = X_{\pi\nu}(\omega)e^{-i\omega t} + Y^*_{\pi\nu}(\omega)e^{i\omega t}, \tag{29b}$$

and, finally, the frequency-dependent perturbed density for an odd nucleus in the EFA is

$$\delta\mathbb{R}(\omega) = \begin{pmatrix} P_{\pi\nu}(\omega) & X_{\pi\nu}(\omega) \\ -Y_{\pi\nu}(\omega) & -Q_{\pi\nu}(\omega) \end{pmatrix}. \tag{30}$$

The use of the EFA ensemble doubles the number of pnFAM equations, from two to four:

$$X_{\pi\nu}(\omega)[(E_\pi + E_\nu) - \omega] = -(1 - f_\nu - f_\pi)\left[\delta H^{20}_{\pi\nu}(\omega) + F^{20}_{\pi\nu}\right], \tag{31a}$$

$$Y_{\pi\nu}(\omega)[(E_\pi + E_\nu) + \omega] = -(1 - f_\nu - f_\pi)\left[\delta H^{02}_{\pi\nu}(\omega) + F^{02}_{\pi\nu}\right], \tag{31b}$$

$$P_{\pi\nu}(\omega)[(E_\pi - E_\nu) - \omega] = -(f_\nu - f_\pi)\left[\delta H^{11}_{\pi\nu}(\omega) + F^{11}_{\pi\nu}\right], \tag{31c}$$

$$Q_{\pi\nu}(\omega)[(E_\pi - E_\nu) + \omega] = -(f_\nu - f_\pi)\left[\delta H^{\overline{11}}_{\pi\nu}(\omega) + F^{\overline{11}}_{\pi\nu}\right]. \tag{31d}$$

Equations (31) are coupled through the dependence of the Hamiltonian matrix $\delta\mathbb{H}(\omega)$ on the perturbed density $\delta\mathbb{R}(\omega)$. In addition to the two "core" equations for X and Y, which are modified from Eq. (12), the EFA pnFAM includes equations for the matrices P (31c) and Q (31d), which describe transitions of the odd quasiparticle(s).

The EFA pnFAM equations are actually no more difficult to solve than the usual ones. Equation (31) contains the additional matrices labeled 11 and $\overline{11}$, but, because we solve for $\mathbb{H}$ iteratively in the single-particle basis and then transform to the quasiparticle basis [18], we multiply by the Bogoliubov matrix $\mathbb{W}$ in Eq. (3) to obtain these additional matrices. A few more iterations may be needed to solve the linear response equations, but that does not significantly increase computation time.

We compute the strength function in odd nuclei in the same way as in even ones, but because $\delta\mathbb{R}(\omega)$ is not block antidiagonal, the valence nucleon(s) affects $S(F;\omega)$ explicitly through P and Q, as well as implicitly through X and Y:

$$\begin{aligned} S(F;\omega) = \sum_{\pi\nu} \big[& F^{20*}_{\pi\nu} X_{\pi\nu}(\omega) + F^{02*}_{\pi\nu} Y_{\pi\nu}(\omega) \\ & + F^{11*}_{\pi\nu} P_{\pi\nu}(\omega) + F^{\overline{11}*}_{\pi\nu} Q_{\pi\nu}(\omega)\big]. \end{aligned} \tag{32}$$

Equation (32) can be obtained directly from the EFA expectation value $\mathrm{Tr}[\hat{F}^\dagger\hat{\mathcal{D}}(t)]/\mathrm{Tr}[\hat{\mathcal{D}}(0)]$ (cf. Refs. [18,29,30]) by requiring that $\delta\hat{\mathcal{D}}(t)$ vary sinusoidally. With the EFA ensemble, $S(F;\omega)$ is simply the average transition strength from the equally occupied odd-A ground states $\alpha^\dagger_\Lambda|\Phi\rangle$ and $\alpha^\dagger_{\bar{\Lambda}}|\Phi\rangle$:

$$S(F;\omega) = \tfrac{1}{2}[S_\Lambda(F;\omega) + S_{\bar{\Lambda}}(F;\omega)]. \tag{33}$$

[See Eq. (19).] The two EFA states include the polarization of the core because of the valence nucleon, at least partially [19].

In Fig. 1, we plot the total Gamow-Teller strength function for the proton-odd nucleus ^{71}Ga. (In our EFA calculation, ^{71}Ga has a slight deformation $\beta_2 = -0.007$; our methods for extracting laboratory-frame transition strength from a deformed intrinsic nuclear ensemble are presented in the appendix). The top panel compares the strength functions

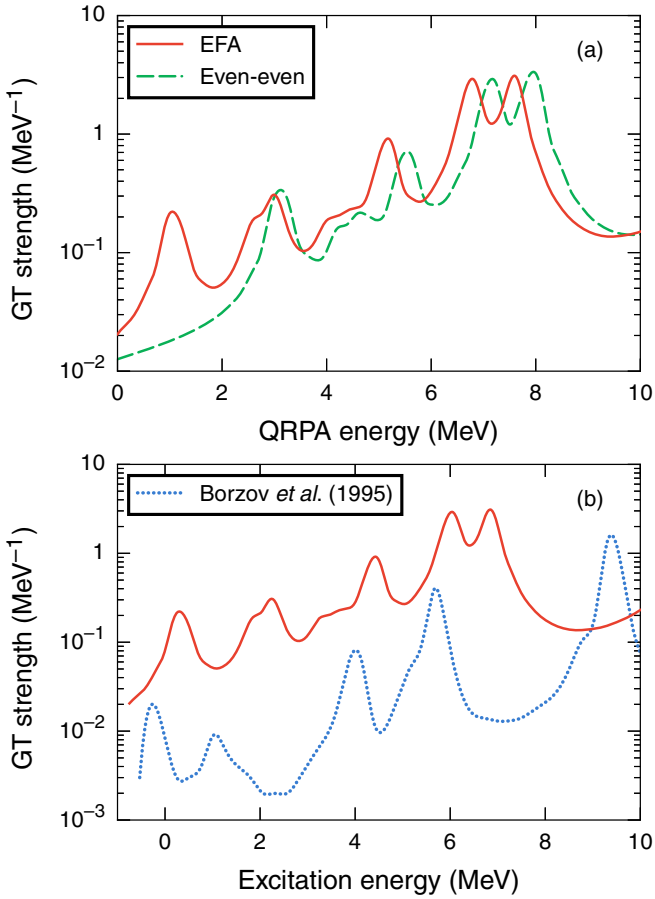

FIG. 1. (Top panel) Gamow-Teller transition strength for ^{71}Ga, computed with the EFA pnFAM (red, solid lines) and the even-even pnFAM with the underlying HFB state constrained to have the correct odd average particle number, as in Ref. [45] (green, dashed lines). (Bottom panel) The same EFA pnFAM strength function as in the top panel, plotted versus excitation energy $E_{\rm ex} = E_{\rm QRPA} - E_0({\rm pn})$ [see Eqs. (34) and (38)], alongside the strength function from Ref. [46] (blue, dotted line).

obtained with the EFA pnFAM and the even-even pnFAM, artificially constrained to obtain the correct odd particle number as suggested in Ref. [45]. The two calculations apply the same Skyrme energy-density functional (SV-min) without proton-neutron isoscalar pairing, but begin with distinct HFB calculations. The EFA calculation clearly includes important one-quasiparticle transition strength near $E_{\rm QRPA} = 1$ MeV that is not present in the other calculation. The bottom panel compares the EFA-pnFAM strength, this time as a function of excitation energy in the daughter nucleus [shifted downward in energy by $E_0({\rm pn}) \simeq 749$ keV—see Eq. (38) and the discussion around Eq. (34)] with a finite Fermi system calculation from Ref. [46]. Although the two calculations do not yield identical strength functions, they clearly mirror one another, and both include low-energy one-quasiparticle strength.

Finally, the odd-A formalism of Ref. [47], used by the authors of Ref. [17], is an approximate version of ours. We would recover similar expressions to those in Ref. [47] by substituting a separable Gamow-Teller interaction for the Skyrme interaction and dropping terms beyond leading order in $P_{\pi\nu}$ and $Q_{\pi\nu}$.

C. Application to β decay in deformed nuclei

Reference [18] discusses the calculation of β-decay rates from pnFAM strength functions at length, so we make only a few important points here. First, we treat the quenching of Gamow-Teller strength by using an effective value $g_A = -1.0$ for the axial-vector coupling constant, in both allowed and first-forbidden β-decay transitions. This renormalization is slightly different from that in Ref. [33], where only Gamow-Teller transitions were quenched. Second, we apply the Q-value approximation of Ref. [7]:

$$Q_\beta = \Delta M_{n-H} + \lambda_n - \lambda_p - E_0({\rm pn}). \tag{34}$$

Here ΔM_{n-H} is the neutron-hydrogen mass difference, the λ_q are Fermi energies, and E_0(pn) is the energy of the lowest two-quasiparticle state for even-even nuclei, or the smallest one-quasiparticle transition energy for odd nuclei. We approximate E_0(pn) with one-quasiparticle energies from the HFB solution; this choice affects only Q_β, not the size of the QRPA energy window, which is determined as in Ref. [18]:

$$E^{\rm max}_{\rm QRPA} = Q_\beta + E_0({\rm pn}) = \lambda_n - \lambda_p + \Delta M_{n-H}. \tag{35}$$

Our procedure for going from the intrinsic frame to the laboratory frame, generalized to include the odd-A EFA ensemble, is described in the Appendix.

III. HALF-LIFE CALCULATIONS

A. Identification of important nuclei

To identify the most important β-decay rates for weak and rare-earth r-process nucleosynthesis, we turn to two sets of nucleosynthesis sensitivity studies. Reference [4] reviews sensitivity studies for main r processes; our studies here proceed as described in Refs. [5,48,49] and Sec. 5.2 of the review, Ref. [4].

The rare-earth peak is formed in a main r process, so for our first set of studies we begin with several choices of astrophysical conditions that produce a good match to the solar r-process pattern for $A \gtrsim 120$. These conditions include hot and cold parametrized winds, similar to those that may occur in core-collapse supernovae or accretion disk outflows, along with mildly heated neutron star merger ejecta. We run a baseline simulation for each astrophysical trajectory (i.e., condition) chosen, and then repeat it with individual β-decay rates changed by a small factor K. Individual β-decay half-lives in the rare-earth region tend to produce local changes to the final abundance pattern that influence the size, shape, and location of the rare-earth peak. Thus we compare the final abundances with those of the baseline simulation by using a local metric $f_{\rm local}$, defined as

$$f_{\rm local}(Z,N) = 100 \times \sum_{A=150}^{180} |Y_K(A) - Y_b(A)|, \tag{36}$$

where Y_b is the final baseline isotopic abundance, and Y_K is the final abundance in a simulation in which the β-decay rate

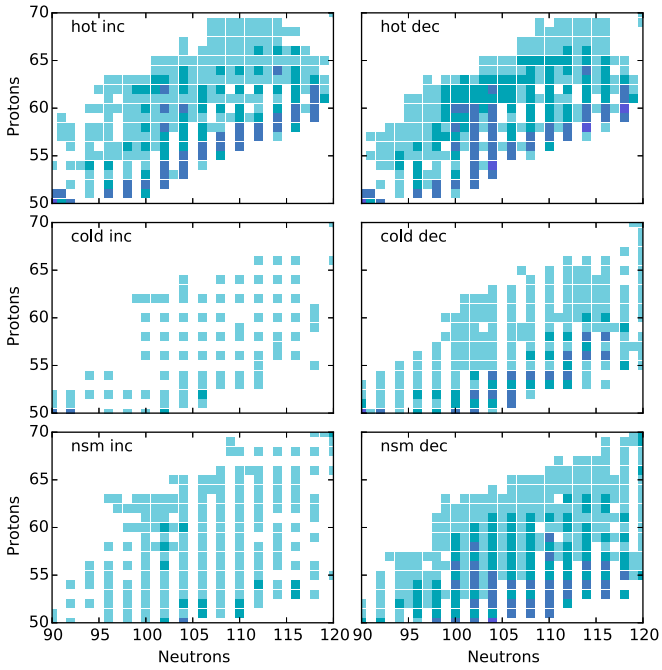

FIG. 2. Influential β-decay rates in the rare-earth region for hot, cold, and merger r-process conditions. The hot conditions are parametrized as in Ref. [50] with entropy $s/k = 200$, dynamical time scale $\tau_{\rm dyn} = 80$ ms, and initial electron fraction $Y_e = 0.3$; the cold conditions are parametrized as in Ref. [51] with $s/k = 150, \tau_{\rm dyn} = 20$ ms, and $Y_e = 0.3$; and the merger conditions are from a simulation of A. Bauswain and H.-Th. Janka, similar to that of Ref. [52]. We performed two sensitivity studies for each trajectory, looking at the results of increases and decreases to the rates by a factor of $K = 5$. In order of lightest to darkest, the shades are white ($f_{\rm local} = 0$), light blue ($0.1 < f_{\rm local} \leqslant 0.5$), medium blue ($0.5 < f_{\rm local} \leqslant 1.0$), dark blue ($1 < f_{\rm local} \leqslant 5$), and darkest blue ($f_{\rm local} > 5$).

of the nucleus with Z protons and N neutrons is multiplied by a factor K. Results for six studies, in which individual β-decay rates were changed by a factor of $K = 5$, with hot, cold, and neutron star merger r-process conditions appear in Fig. 2. The largest impacts on the final abundances occur near the peak ($A \sim 160$), although which nuclei are most sensitive depends a little on the astrophysical conditions chosen.

In the second set of studies, focused on the $A \sim 80$ peak, we start with a baseline weak r-process simulation that produces an abundance pattern with a good match to the solar pattern for $70 < A < 110$, as identified in Ref. [49]. Here we choose conditions qualitatively similar to those found in the outflows of neutron star or neutron star-black hole accretion disks [53,54], which are attractive candidate sites for the weak r process. We run a sensitivity study as described above, varying each β-decay lifetime in turn by a factor of $K = 10$ and comparing the result to the baseline pattern. Unlike in the rare-earth region, where the influence of an individual β-decay rate is primarily confined to the surrounding nuclei, rates in the peak regions can produce global changes to the pattern [5] and can influence how far the process proceeds in A. Thus, in this study we compare each pattern to the baseline with a

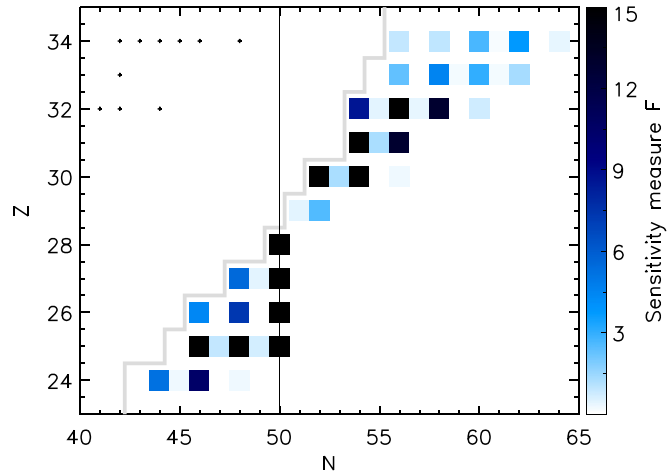

FIG. 3. Influential β-decay rates in the $A \sim 80$ region for weak r-process conditions, parametrized as in Ref. [50] with entropy per baryon $s/k = 10$, dynamic time scale $\tau = 200$ ms, and starting electron fraction $Y_e = 0.3$. The shaded boxes show the global sensitivity measures $F_{\rm global}$ resulting from β-decay rate increases of a factor of $K = 10$. Stability is indicated by crosses; the β-decay rates of nuclei to the right of stability and to the left of the solid gray line have all been measured and so are not included in the sensitivity analysis.

global sensitivity measure $F_{\rm global}$:

$$F_{\rm global} = 100 \times \sum_A |X_K(A) - X_b(A)|, \qquad (37)$$

where $X_b(A)$ and $X_K(A)$ are the final mass fractions of the baseline simulation and the simulation with the β-decay rate changed, respectively. Figure 3 shows representative results. The pattern of most influential β-decay lifetimes is similar to that identified for a main r process [5]: The important nuclei tend to be even-N isotopes along either the r-process path or the decay pathways of the most abundant nuclei.

We select isotopic chains with the highest sensitivity measures, according to Figs. 2 and 3, and carefully recalculate their β-decay half-lives. The selected chains encompass 70 nuclei in the rare-earth region and 45 nuclei in the $A \sim 80$ region.[1]

B. Selection and adjustment of Skyrme EDFs

Our density-dependent nucleon-nucleon interactions are derived from Skyrme EDFs. References [56–58] contain comprehensive reviews of the properties of Skyrme functionals; Refs. [18,33] contain discussions of the most important terms of the EDF for β decay. In our calculations, we largely apply the Skyrme EDF "as is," but adjust a few important parameters that affect ground-state properties and β-decay rates. Among these are the proton and neutron like-particle pairing strengths V_p and V_n; the spin-isospin coupling constant C_{10}^s; and the

[1]Measured half-lives of ^{76,77}Co and ^{80,81}Cu were recently reported in Ref. [55]. We still include these nuclei in our calculations.

proton-neutron isoscalar pairing strength V_0. We tune these parameters separately for each mass region; the coupling constants that multiply the remaining "time-odd" terms of the Skyrme EDF are set either to values determined by local gauge invariance [58] or to zero. Though our pnFAM code is able to handle tensor interactions [18], none of the EDFs we use here have nonzero tensor couplings C_t^F or $C_t^{\nabla s}$ (in the notation of Refs. [18,59]).

1. *Multiple Skyrme EDFs for the rare-earth elements*

The pnFAM's efficiency significantly reduces the computational effort in β-decay calculations. The smaller computational cost makes repeated calculations feasible and allows us to examine the extent to which β-decay predictions depend on the choice of Skyrme EDF. Here we use four very different Skyrme functionals: SkO′ [60], SV-min [61], UNEDF1-HFB [62], and SLy5 [63]. SkO′ was already applied to the β decay of spherical nuclei [7]; it was also chosen for the recent global calculations of Ref. [33]. SV-min and UNEDF1-HFB are more recent; the latter is a re-fit of the UNEDF1 parametrization [64], without Lipkin-Nogami pairing. SLy5 tends to yield less-collective Gamow-Teller strength than some other Skyrme parametrizations [65].

We do most of our calculations in a 16-shell harmonic oscillator basis, a choice that further reduces computational time from that associated with the 20-shell basis applied in the UNEDF parametrizations of Refs. [64,66,67]. Because UNEDF1-HFB was constructed with HFBTHO in a 20-shell basis, however, we use this larger basis for that particular functional. We determine the nuclear deformation by starting from three trial shapes (spherical, prolate, and oblate) and selecting the most bound result after the HFB energy and deformation have been determined self-consistently. We obtain the mean-field ground states of odd nuclei within the EFA, beginning from a reference even-even solution and then computing odd-A solutions for a list of blocking candidates reported by HFBTHO. For odd-odd nuclei, we try all $N_p \times N_n$ proton-neutron configurations to take into account as many odd-odd trial states as are practical. Again, we select the most-bound quasiparticle vacuum from among these candidates.

Returning to the functionals themselves, to adjust the pairing strengths and coupling constant C_{10}^s, we start from the published parametrizations.[2] Then we fix the like-particle pairing strengths V_p and V_n by comparing the average HFB pairing gap to the experimental odd-even staggering (OES) of nuclear binding energies for the small set of test nuclei listed in Table I.[3] Following the procedure in Refs. [64,66,67], we adjust the HFB pairing gap to match the indicator (e.g., for neutrons) $\tilde{\Delta}_n^{(3)}(Z,N) = \frac{1}{2}[\Delta_n^{(3)}(Z,N+1) + \Delta_n^{(3)}(Z,N-1)]$ for even-even nuclei. We obtain the usual three-point indicators $\Delta^{(3)}$ [69,70] from mass excesses in the 2012 Atomic Mass Evaluation [71,72]—after using the prescription of Ref. [72] to remove the electron binding [66] from the atomic binding energies [73]. After finding pairing strengths that correspond to one-σ uncertainties in $\tilde{\Delta}^{(3)}$(treating asymmetric uncertainties as in Ref. [74]), we find best-fit values V_p and V_n for our sample set of nuclei. For all EDFs except SV-min, we choose mixed volume-surface pairing, with $\alpha = 0.5$ as in Ref. [18]. SV-min's pairing piece was originally fixed along with the rest of the functional, but in the HF+BCS framework. We therefore refit the pairing strengths to better represent ground-state properties with HFBTHO, keeping the coefficient that specifies density dependence at its value of $\alpha = 0.75618$ from Ref. [61].

TABLE I. OES indicators $\tilde{\Delta}^{(3)}$ for the even-even nuclei used to fit the pairing strengths V_p and V_n.

Z	N	$\tilde{\Delta}_p^{(3)}$ (MeV)	$\tilde{\Delta}_n^{(3)}$ (MeV)
52	84	0.79096 ± 0.00464	0.75491 ± 0.0024
54	86	0.90975 ± 0.01527	0.87276 ± 0.0022
56	90	0.92059 ± 0.01093	0.92025 ± 0.0204
58	90	0.99503 ± 0.00975	0.97777 ± 0.0092
60	92	0.68605 ± 0.01176	0.77895 ± 0.0298
62	94	0.57543 ± 0.02887	0.67368 ± 0.0042
62	96	0.55867 ± 0.05021	0.58183 ± 0.0049
64	96	0.57608 ± 0.00276	0.67969 ± 0.0018
66	98	0.53795 ± 0.00277	0.67866 ± 0.0016
68	100	0.55392 ± 0.00312	0.64734 ± 0.0017
68	102	0.50391 ± 0.03646	0.60222 ± 0.0021
70	104	0.52725 ± 0.00300	0.53483 ± 0.0017
72	106	0.62796 ± 0.00168	0.63470 ± 0.0016
72	108	0.62486 ± 0.00388	0.57799 ± 0.0022
74	110	0.55784 ± 0.00199	0.66483 ± 0.0008
74	112	0.60795 ± 0.01224	0.70165 ± 0.0013
74	114	0.67773 ± 0.03607	0.79595 ± 0.0227
76	116	0.78248 ± 0.01110	0.83218 ± 0.0020
78	118	0.75364 ± 0.00128	0.88139 ± 0.0009

Next, we determine an appropriate value for C_{10}^s by comparing the excitation energy,

$$E_{\rm ex} = E_{\rm QRPA} - E_0({\rm pn}), \tag{38}$$

of the Gamow-Teller giant resonance (GTR) to an experimentally measured value in a nearby nucleus. This constant C_{10}^s is the same one we adjusted to GTR data in the past [18], following the work of Ref. [59]; Ref. [33] recently showed that it is the only particle-hole constant that is truly important for β decay. In these $A \simeq 160$ nuclei, we use the resonance associated with the doubly magic nucleus ^{208}Pb, with $E_{\rm ex} = 15.6 \pm 0.2$ MeV in the odd-odd daughter ^{208}Bi [75], to fix it. We also use the deformed rare-earth nucleus ^{150}Nd ($E_{\rm ex} \simeq 15.25$ MeV in ^{150}Pm [76]), to fix an alternative value C_{10}^s in SkO′, calling the resulting functional SkO′-Nd. The two fits result in values of C_{10}^s that differ by nearly 20%. Figure 4 compares the Gamow-Teller strength functions produced by the two values in ^{150}Pm. Not only are the

[2]With a few exceptions, we use the same nucleon mass for proton and neutrons, unlike Ref. [61], which originally determined SV-min, and we employ the SLy5 parametrization written into HFBTHO, which differs from that published in Ref. [63]. The HFBTHO values are the same as those of Ref. [68], but $t_0 = -2483.45$ MeV fm^3 instead of -2488.345 MeV fm^3.

[3]The UNEDF1-HFB pairing strengths were originally fit simultaneously with the rest of the functional (with HFBTHO), so we do not readjust the UNEDF1-HFB pairing strengths.

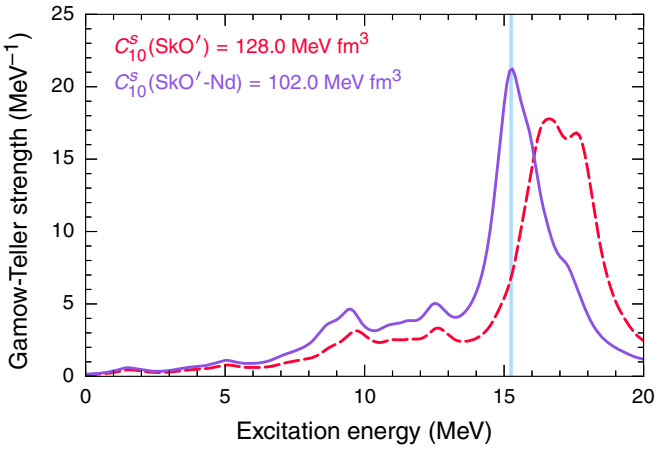

FIG. 4. Gamow-Teller strength functions in ^{150}Pm for SkO′ (red dashed line, with C^s_{10} fit to the GTR energy in ^{208}Pb) and SkO′-Nd (purple solid line, with C^s_{10} fit to the GTR energy in ^{150}Nd). The vertical line marks the measured GTR energy in ^{150}Pm.

resonances at different places, but there is also a big difference in the strength functions at the low energies that are important for β decay.

To adjust the $T = 0$ pairing, we select short-lived even-even isotopes with $Z = 54$, 56, 58, 60, 62, and 64 with β-decay rates that have been measured reasonably precisely, according to Ref. [77]; the 18 nuclei we use are listed in Table II. For each nucleus, we attempt to find a pairing strength V_0 that reproduces the measured half-life. If a calculated half-life is too short, even when $V_0 = 0$, we remove the nucleus from consideration; This prevents our fit from being influenced by

TABLE II. Isotopes used to fit the proton-neutron isoscalar pairing to experimental half-lives from Ref. [77]. Labels a–e in the "Excluded?" column note which isotopes were excluded from the fits for the functionals (a) SkO′, (b) SkO′-Nd, (c) SV-min, (d) SLy5, and (e) UNEDF1-HFB, as discussed in the text.

Z	N	Element	$T_{1/2}$(expt.)	Excluded?
54	88	^{142}Xe	1.23	b d e
54	90	^{144}Xe	0.388	b d e
54	92	^{146}Xe	0.146	d e
56	88	^{144}Ba	11.5	a b d e
56	90	^{146}Ba	2.22	b d e
56	92	^{148}Ba	0.612	e
58	90	^{148}Ce	56	b c d e
58	92	^{150}Ce	4	d e
58	94	^{152}Ce	1.4	d e
60	92	^{152}Nd	684	a b c d e
60	94	^{154}Nd	25.9	b c d e
60	96	^{156}Nd	5.06	b d e
62	96	^{158}Sm	318	a b c d e
62	98	^{160}Sm	9.6	e
62	100	^{162}Sm	2.4	e
64	98	^{162}Gd	504	b e
64	100	^{164}Gd	45	e
64	102	^{166}Gd	4.8	e

TABLE III. Summary of proton-neutron $T = 0$ pairing fit, including the amount of test data in each fit (N) and the resulting pairing strength (V_0).

EDF	N	V_0
SkO′	15/18	−320.0
SV-min	14/18	−370.0
SkO′-Nd	9/18	−300.0
SLy5	6/18	−240.0
UNEDF1-HFB	0/18	−0.0

especially long-lived or sensitive isotopes. After determining an approximate $V_0 \neq 0$ for each nucleus (where possible), we compute the average of these values, weighing fast decays more than slow ones (because the very neutron-rich r-process nuclei are short-lived), with weight factors,

$$w_i = \frac{1}{\log_{10}\left[T^{\rm expt}_{1/2}(i)/35\ {\rm ms}\right]}. \tag{39}$$

The fit is fairly insensitive to the weighting half-life $T_0 = 35$ ms; with $T_0 = 25$ ms the fit values of V_0 change by $\simeq 2\%$.

Table III lists the values for V_0 that we end up with and the number of nuclei incorporated into the fit for each EDF. We find that none of the EDFs predict long-enough half-lives to fix $V_0 \neq 0$ for the entire set of test nuclei; SkO′ (15 of 18) and SV-min (14) come the closest, while SLy5 (only 6) and UNEDF1-HFB (zero) come less close and are thus poorly constrained by β decay. (We discuss SkO′-Nd momentarily.) One cannot really have confidence in fits (SLy5, UNEDF1-HFB) that take into account less than half of the available data, but Fig. 5 provides at least a partial explanation. It compares our calculated Q values (34) to measured values [72] and those of the finite-range droplet model in Ref. [6]. Our Q values are almost uniformly larger than experiment (those of Ref. [6] are generally smaller), and those of SLy5 and UNEDF1-HFB are much larger. Because the β-decay rate is roughly proportional to Q^5 [78], a Q value that is too large will lead to an artificially

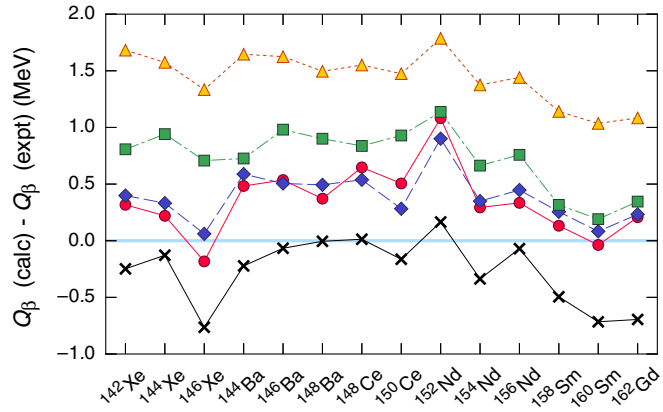

FIG. 5. The difference between calculated and experimental β-decay Q values, with SkO′ (circles), SV-min (diamonds), SLy5 (squares), and UNEDF1-HFB (triangles). Q values of Ref. [6] (crosses) also appear.

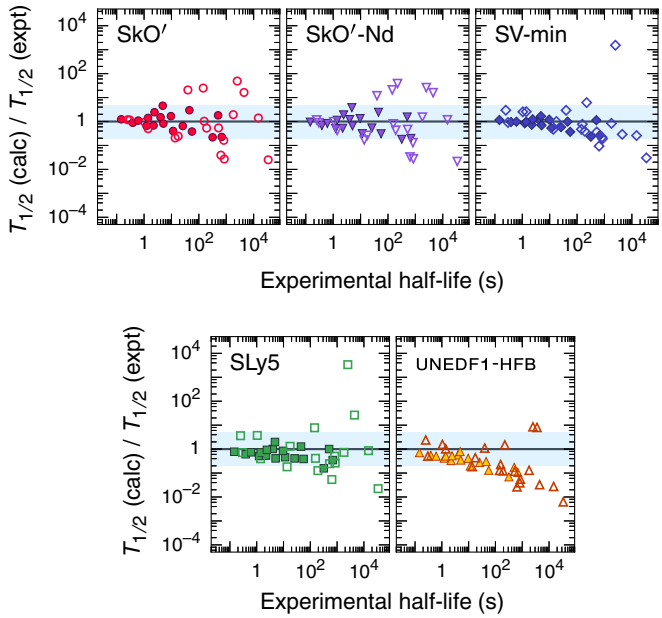

FIG. 6. Performance of fit functionals in even-even rare-earth nuclei. Filled symbols mark nuclei used to fit the $T = 0$ pairing. The experimental data are from Ref. [77].

short half-life. The $T = 0$ pairing only makes the half-lives shorter.

The Q-value fitting difficulties, however, do not manifest themselves in actual half-life predictions as much as they might, even with SLy5 and UNEDF1-HFB. Figure 6 compares our calculations to experimental measurements in the 18 test nuclei used to fit V_0 (listed in Table II) and an additional 18 rare-earth nuclei (listed in Table IV). Our results display the same pattern

TABLE IV. The 18 even-even rare-earth nuclei in Fig. 6 that are not included in the EDF fitting. Experimental half-lives, in seconds, are from Ref. [77].

Z	N	Element	$T_{1/2}$(expt.)
50	84	^{134}Sn	1.05
50	86	^{136}Sn	0.25
52	82	^{134}Te	2508
52	84	^{136}Te	17.63
52	86	^{138}Te	1.4
54	84	^{138}Xe	844.8
54	86	^{140}Xe	13.6
56	86	^{142}Ba	636
56	94	^{150}Ba	0.3
58	90	^{146}Ce	811.2
62	90	^{156}Sm	33840
66	102	^{168}Dy	522
68	106	^{174}Er	192
70	108	^{178}Yb	4440
70	110	^{180}Yb	144
72	112	^{184}Hf	14832
72	114	^{186}Hf	156
74	116	^{190}W	1800

TABLE V. $A \simeq 80$ nuclei used to fit the like-particle pairing strengths. We again use data from Ref. [72] to compute the experimental indicators $\tilde{\Delta}^{(3)}$. We set $\tilde{\Delta}^{(3)} = 0$ for nuclei with $Z = 28$ or $N = 50$.

Z	N	$\tilde{\Delta}^{(3)}_{\rm p}$ (MeV)	$\tilde{\Delta}^{(3)}_{\rm n}$ (MeV)
24	32	1.26354	1.01634
26	38	1.17387	1.29269
30	44	1.01199	1.41433
32	46	1.13235	1.24835
32	48	0.99635	1.17779
34	52	1.17100	0.78968
36	54	1.15773	0.83990
36	56	1.18243	0.90644
38	58	1.11437	0.93063
38	60	0.99089	0.85591
42	62	0.99786	0.95077
28	38	0.00000	1.20975
32	50	0.95788	0.00000
28	50	0.00000	0.00000

as many others (e.g., Refs. [17,45,79]), reproducing half-lives of short-lived nuclei better than those of longer-lived ones. The Q-value errors discussed previously show up as systematic biases in our half-life predictions (particularly with SLy5 and UNEDF1-HFB, for which half-lives of long-lived nuclei are artificially reduced). The shortest-lived nuclei, however, are not so poorly represented even with SLy5 and UNEDF1-HFB; these half-lives are still systematically short but by less than a factor of about two (the shaded region in Fig. 6 covers a factor of 5 relative to measured values). The systematic problems in the two functionals based on SkO′ are barely noticeable. SV-min, which performs the best overall, is somewhere in the middle. Because all the functionals do well with the short-lived isotopes, we use them all for our rare-earth calculations. The lifetimes we get with UNEDF1-HFB serve as lower bounds on our predictions.

Finally, although SkO′-Nd, the SkO′ variant that reproduces the GTR in ^{150}Nd, fails in 9 of the 18 nuclei used for fitting, its predictions do not differ significantly from those of SkO′. Figure 4 shows increased low-energy Gamow-Teller transition strength as C^s_{10} is reduced to reproduce the rare-earth GTR. This increased low-lying strength reduces β-decay half-lives so that a smaller pairing strength is required (see Table III), with no loss of quality.

2. *Weak r-process elements*

To calculate the half-lives of $A \simeq 80$ nuclei, we elect to apply the functional from the previous section that best reproduces measured half-lives. Both Fig. 6 and the metrics in Ref. [17] point to SV-min as the best EDF. We adjust SV-min for these lighter nuclei in much the same way as discussed in the previous section. We fit the like-particle pairing to calculated OES values (see Table V), this time employing the fitting software POUNDerS [80] to search for the best values of V_p and V_n. We provide POUNDerS with the weighted residuals,

$$X_i = w_i\left[\bar{\Delta}_i(V_p, V_n) - \tilde{\Delta}^{(3)}_i\right], \tag{40}$$

TABLE VI. Open-shell (top) and semimagic (bottom) even-even $A \simeq 80$ nuclei whose half-lives are used to adjust the proton-neutron isoscalar pairing. Experimental half-lives are from the ENSDF [82].

Z	N	Isotope	$T_{1/2}$ (s)
22	38	^{60}Ti	0.022
24	40	^{64}Cr	0.043
26	44	^{70}Fe	0.094
30	52	^{82}Zn	0.228
32	52	^{84}Ge	0.954
34	54	^{88}Se	1.530
36	60	^{96}Kr	0.080
28	46	^{74}Ni	0.680
28	48	^{76}Ni	0.238
30	50	^{80}Zn	0.540
32	50	^{82}Ge	4.560

where $\bar{\Delta}_i$ is the average HFB pairing gap for the ith nucleus and the weight factor w_i is 1 for nonmagic nuclei and 10 for magic ones. The search yields $V_p = -361.0\,\text{MeV fm}^3$ and $V_n = -320.9\,\text{MeV fm}^3$. We adjust the coupling constant C^s_{10} to the GTR in a lighter doubly magic nucleus, ^{48}Ca ($E_{\text{ex}} =$ 10.6 MeV in ^{48}Sc [81]).

Finally, as before, we adjust the $T = 0$ pairing strength to reproduce measured half-lives of even-even nuclei, now with $A \simeq 80$ (see Table VI). In this region of the isotopic chart the fit is complicated by the presence of both proton and neutron closed shells (see Fig. 3), so we include $Z = 28$ and $N = 50$ semimagic nuclei in the fit. Figure 7 shows the impact of the $T = 0$ pairing on half-lives and in particular in the difference in the effect between nonmagic nuclei (solid lines) and semimagic nuclei (dashed lines). We search for distinct values of V_0 for these two cases, finding $V_0(\text{nm}) = -353.0\,\text{MeV fm}^3$ for nonmagic nuclei and $V_0(\text{sm}) = -549.0\,\text{MeV fm}^3$ is for our set of semimagic nuclei.

The top panel of Fig. 8 shows the results of these adjustments, comparing calculated β-decay half-lives of even-even (left panel) and singly odd (right) nuclei with measured values

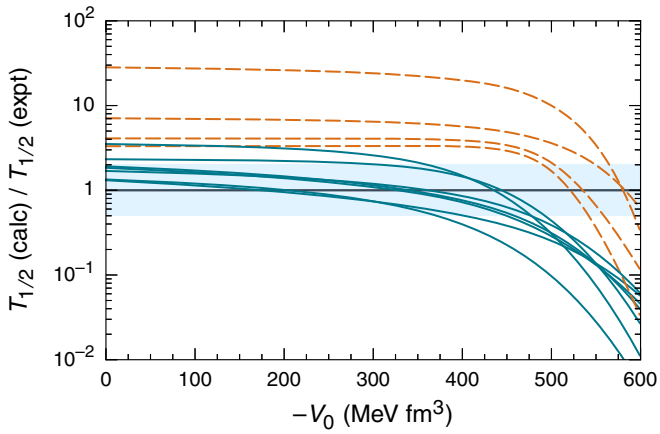

FIG. 7. Impact of $T = 0$ pairing on β-decay half-lives, both for nonmagic (solid lines) and semimagic (dashed lines) nuclei. The shaded region marks agreement between our calculation and measured half-lives [82] to within a factor of two.

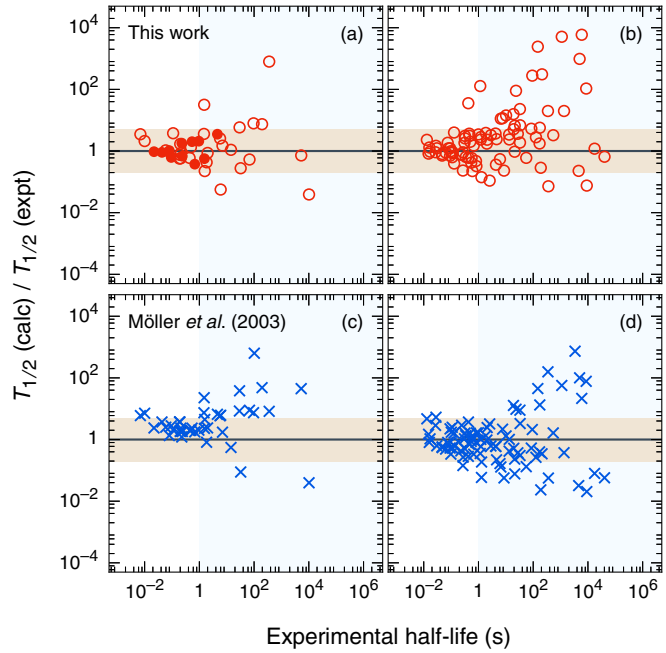

FIG. 8. Performance of our SV-min calculations (top panels) and the FRDM calculations of Ref. [17] (bottom panels) for nuclei with $22 < Z < 36$ and $T_{1/2} \leqslant 1$ day. Left panels show the ratio of calculated to measured half-lives in even-even nuclei; right panels show the ratio in odd-A nuclei. Filled circles in the upper-left panel denote even-even nuclei used to fit the $T = 0$ proton-neutron pairing. The shaded horizontal band marks agreement to within a factor of five, and the white background on the left side marks nuclei with measured half-lives that are shorter than 1 s.

[82], for nuclei with $22 < Z < 36$ and $T_{1/2} < 1$ day. The bottom panel shows the same comparison for the finite-range droplet model (FRDM) calculation of Ref. [17]. The two sets of results are comparable, but those of Ref. [17] have a clear bias in even-even nuclei. A metric defined in Ref. [17],

$$r_i = \log_{10}\left[\frac{T^{\text{calc}}_{1/2}(i)}{T^{\text{expt}}_{1/2}(i)}\right], \tag{41}$$

captures the bias. The mean and RMS deviation of 10^{r_i}, called M^{10}_r and Σ^{10}_r, quantify the deviation between calculation and experiment: A value $M^{10}_r = 2$ would signify that calculations produce half-lives that are too long by a factor of two, on average. Our calculated rates yield $M^{10}_r = 1.32$ in even-even nuclei while those of Ref. [17] give $M^{10}_r = 3.55$. For the standard deviation, our rates yield $\Sigma^{10}_r = 5.14$, vs 7.50 for those of Ref. [17]. Thus, we indeed do measurably better in even-even nuclei. Our results in odd-A nuclei are worse than those of Ref. [17], however; we obtain $M^{10}_r = 2.71$ (vs 0.95) and $\Sigma^{10}_r = 11.61$ vs (6.46). The two sets of calculations are comparable for short-lived odd-A nuclei, however: We get $M^{10}_r = 1.11$ vs 0.96 and $\Sigma^{10}_r = 2.48$ vs 2.21 for isotopes with $T_{1/2} \leqslant 1$ s.

C. Results near $A = 160$

Guided by the sensitivity studies in Fig. 2, we identify 70 rare-earth nuclei, all even even or proton odd, with rates that

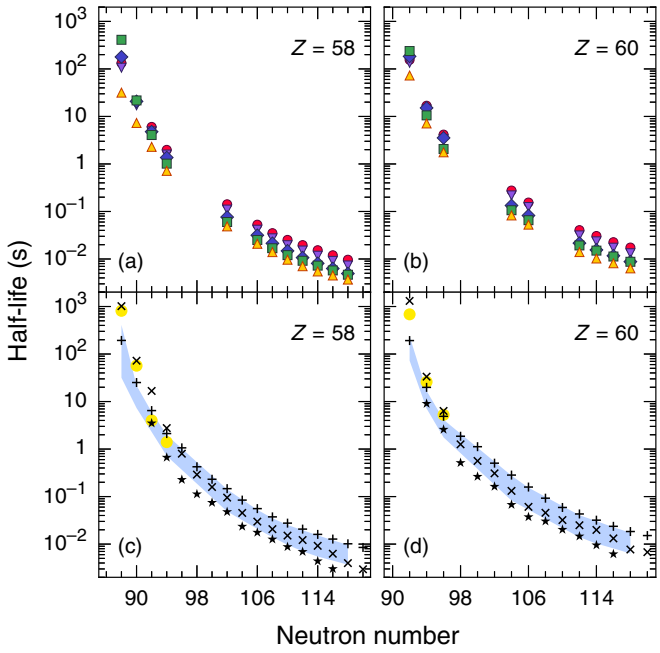

FIG. 9. (Top panels) Half-lives for nuclei in the Ce ($Z = 58$, left) and Nd ($Z = 60$, right) isotopic chains, calculated with the Skyrme EDFs described in the text. Symbols correspond to the same EDFs as in Fig. 6. (Bottom panels) Calculated half-lives of Ref. [17] ($\times$), [33] ($+$), and [83] ($\star$), measured half-lives [82] (circles), and the range of half-lives reported in this paper (shaded region).

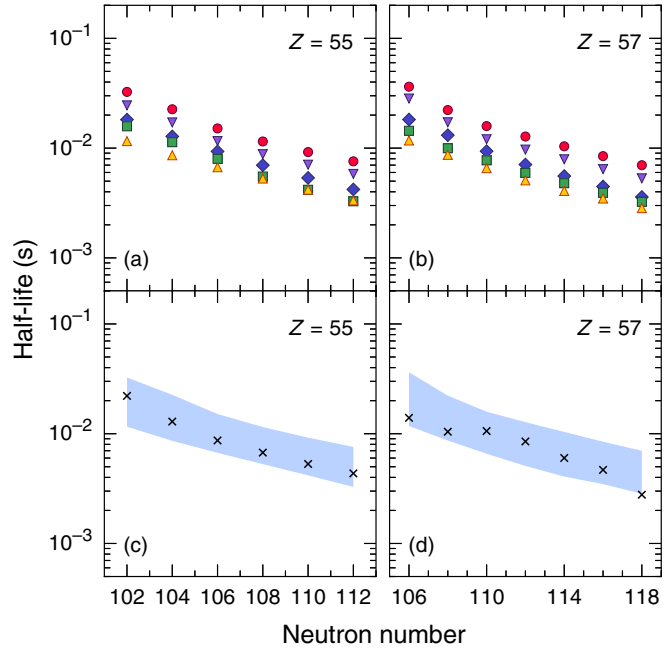

FIG. 10. (Top panels) Half-lives for nuclei in the Cs ($Z = 55$, left) and La ($Z = 57$, right) isotopic chains, calculated with the Skyrme EDFs described in the text. Symbols correspond to the same EDFs as in Figs. 6 and 9. (Bottom panels) Calculated half-lives from Ref. [17] ($\times$) superimposed upon the range of half-lives reported in this paper (shaded region).

strongly affect r-process abundances near $A = 160$. (Neutron-odd nuclei do not significantly affect the r process because they quickly capture neutrons to form even-N isotopes [1].) Figures 9 and 10 present new calculated half-lives in four isotopic chains, with even-Z isotopes in Fig. 9 and odd-Z isotopes in Fig. 10. The top panels of these figures include predictions with all five adjusted Skyrme EDFs, and the bottom panels compare our calculations to measured values [82] and the results of previous QRPA calculations [17,33,83] where they are available. Our calculations span the (narrow) range of predicted half-lives in these isotopic chains, with SLy5 and UNEDF1-HFB predicting the shortest half-lives for the most neutron-rich isotopes, as one could expect from the analysis of Sec. III B 1. While the UNEDF1-HFB half-lives are uniformly short, however, those of SLy5 actually are the longest predictions (and the closest to measured values) for nuclei nearer to stability. The variability of our half-life predictions in Figs. 9 and 10 is typical of all 70 nuclei in the calculation. The longest and shortest calculated half-lives for any nucleus in our set differ by a factor ranging from about 1.9 to 3.3, and this interval does not depend strongly on whether a nucleus has an even or odd number of protons.

The results of Refs. [17,33,83] are actually fairly similar to ours, spanning roughly the full range of our predicted values in Fig. 9. (Neither Ref. [33] nor [83] report half-lives for odd-Z nuclei and so cannot be a part of Fig. 10.) The half-lives of Ref. [33] are close to our own SkO′ half-lives, a result that is unsurprising given that the EDF in that paper is a modified version of SkO′ (and that we use the same pnFAM code). The half-lives of Ref. [17] lie, for the most part, right in the middle of our predictions and follow those of SV-min fairly closely (the Q values are similar). Finally, Fang's recent calculations [83] yield relatively short half-lives, shorter than even those of UNEDF1-HFB most of the time. Still, the band of predicted half-lives is relatively narrow among these three calculations even in the most neutron-rich nuclei. Reference [33] points out that despite their differences, most global QRPA calculations produce comparable half-lives. Our results in both $A \simeq 80$ and $A \simeq 160$ nuclei support this observation.

Figures 9 and 10 (as well as Fig. 11, discussed momentarily) show that the overall pattern of β decays in the $A \simeq 160$ region

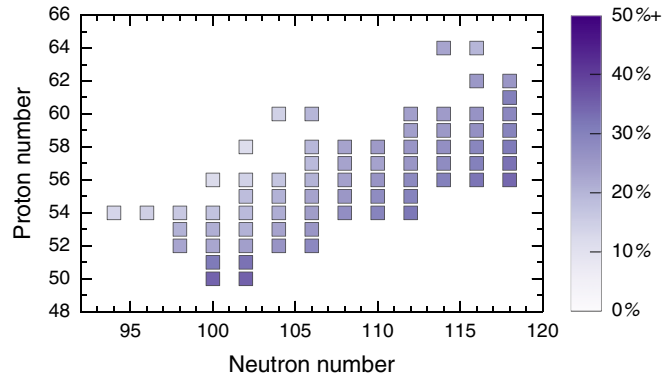

FIG. 11. Impact of first-forbidden β transitions in rare-earth nuclei that are important for the r-process nuclei, with the Skyrme EDF SV-min.

does not depend much on whether an element has an even or odd number of protons. As mentioned above, the variability in predictions is approximately equal for these two classes of nuclei, and we see in Fig. 10 that the calculations of Ref. [17] continue to lie toward the middle of our predictions. We also find that our calculations for both even-even and odd-Z nuclei predict smoothly decreasing in half-lives (on a logarithmic scale) with increasing neutron number. In this respect our calculations differ slightly from those of Ref. [17], the results of which are more variable (a fact most easily seen in Fig. 10).

Finally, we have examined the impact of first-forbidden β decay on half-lives of rare-earth nuclei. Figure 11 shows that in heavier nuclei forbidden decay makes up between 10% and 40% of the total decay rate. The percentage generally increases with A.

D. Results near $A = 80$

Following the weak r-process sensitivity study in Fig. 3, we present new half-lives for 45 $A \simeq 80$ nuclei in Fig. 12, comparing our results to those of Refs. [17,33]. Not surprisingly, in light of Fig. 8, our calculated half-lives (circles) are often slightly shorter than those of Ref. [17] (crosses). They are also similar to those of Ref. [33], which used the same pnFAM code for even-even nuclei. We have also compared our $A \simeq 80$ half-lives to those of the QRPA calculations in Ref. [79], finding very similar results for the few isotopic chains discussed both here and there.

One interesting feature of our calculation is that the half-lives of ^{85,86}Zn, ^{89}Ge, and (to a lesser extent) ^{90}As are long compared to those of Ref. [17]. The top panel of Fig. 13, which plots our calculated quadrupole deformation β_2 for $A \simeq 80$ nuclei, suggests these longer half-lives are at least partially from changes in ground-state deformation. The Zn isotopes switch from being slightly prolate to oblate near ^{86}Zn ($N = 56$), while Ge and As isotopes do the same near $N = 57$. Our calculations find ^{89}Ge to be spherical and situated between two

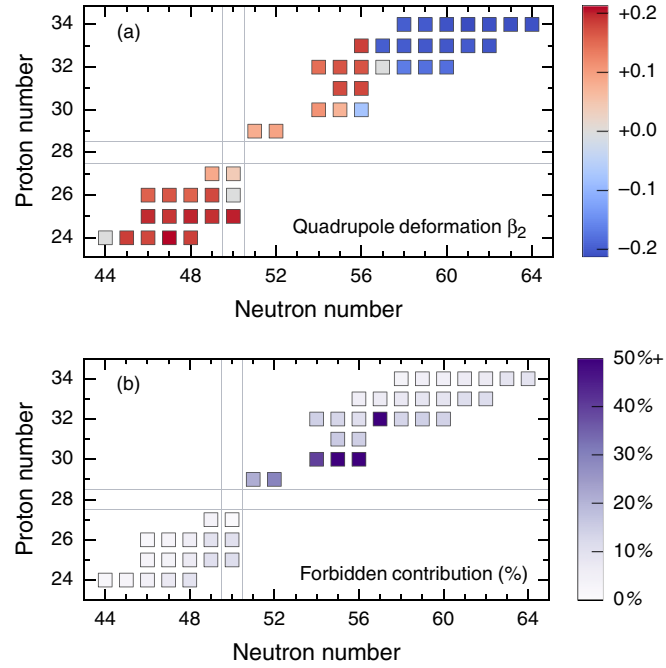

FIG. 13. (Top panel) Quadrupole deformation β_2 of the 45 $A \simeq 80$ nuclei whose half-lives we calculate and display in Fig. 12. (Bottom panel) Contribution of first-forbidden β decay ($0,1,2^-$ transitions) to the decay rate of the same 45 nuclei, plotted as a percentage.

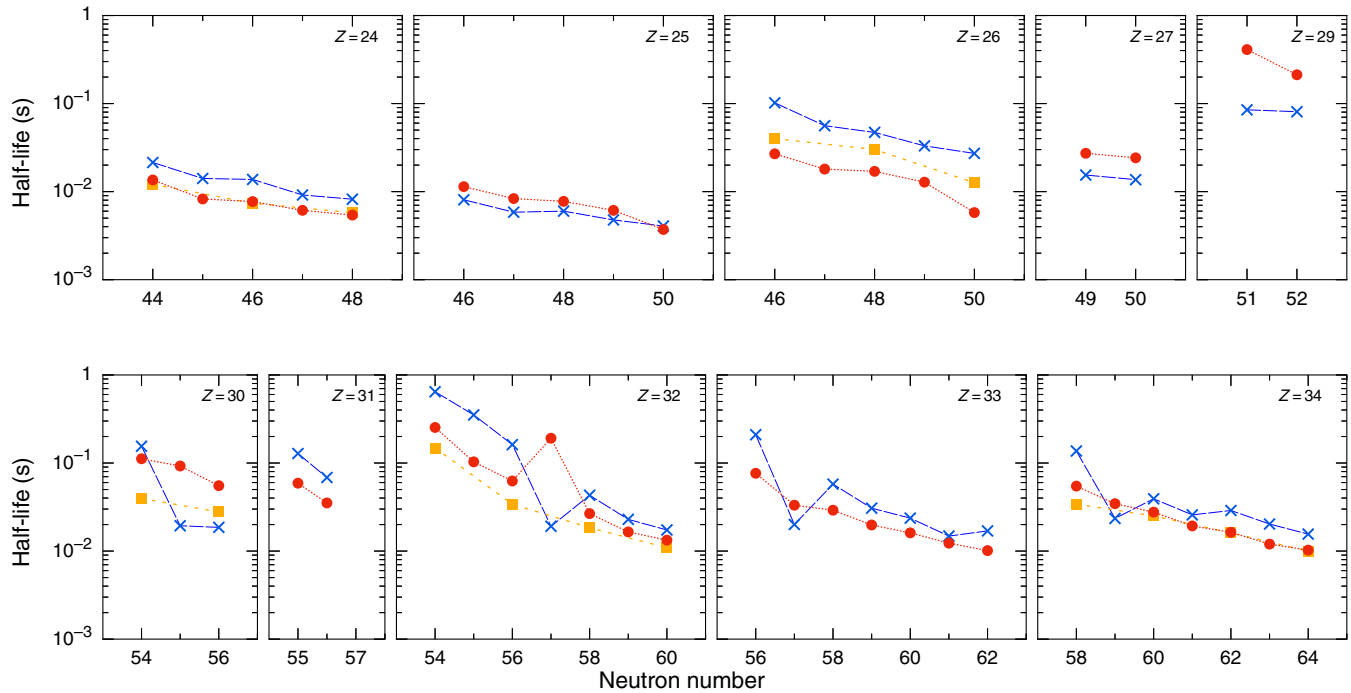

FIG. 12. Computed half-lives in $A \simeq 80$ β decay (red circles), along with those of Refs. [33] (orange squares) and [17] (blue crosses).

isotopes with $\beta_2 \sim \pm 0.17$. The authors of Ref. [17] appear to force $^{83-90}$Ge to be spherical.

The bottom panel of Fig. 13 shows the impact of first-forbidden β decay in this mass region; together with the top panel it connects negative-parity transitions with ground-state deformation. As discussed in Ref. [84], first-forbidden contributions to β-decay rates are small, except in the oblate transitional nuclei discussed above. These results largely agree with those of the recent global calculation in Ref. [33].

We also find that while the most deformed nuclei decay almost entirely via allowed transitions, spherical isotopes show a large scatter in the contribution of forbidden decay. More than 80% of the ^{89}Ge decay rate is driven by first-forbidden transitions. This analysis may bear on the large first-forbidden contributions near $N = 50$ and $Z = 28$ reported by Ref. [45], which restricted nuclei to spherical shapes. Reference [79], which considers the effect of deformation on Gamow-Teller strength functions, suggests that it is important near this mass region.

Our calculations near $A = 80$ include even-even, odd-even, even-odd, and odd-odd nuclei. Though odd pnFAM calculations are no more computationally difficult than even ones, a few odd half-lives are probably a little less reliable than their even counterparts for two (related) reasons. First, we have found that our calculations produce negative contributions to decay rates in some first-forbidden channels of a few nuclei. We simply remove these negative contributions, with the following results: The total β-decay rate of ^{77}Co changes by only 0.1%, ^{80}Cu by 160%, ^{81}Cu by 17%, and ^{97}Se by 6%. Second, we have found that the lowest-energy (unperturbed) charge-changing single-quasiparticle transition lies at an energy $E < 0$ for a few odd nuclei. In other words, there are a few odd-proton nuclei for which $E_\nu - E_\pi < 0$ and a few odd-neutron nuclei for which $E_\pi - E_\nu < 0$. The situation occasionally allows negative QRPA energies. Our technique for calculating the decay rate then fails because of the form of the pnFAM strength function [18]: For every state at $E = \hbar\omega$ that has β^- strength, the pnFAM generates a state with β^+ strength equal to the negative of the β^- strength at $E = -\hbar\omega$. As a result, if there are states with negative energy and nonzero β^- strength, then when we apply the residue theorem to obtain integrated strength [85] we include (the negative of) spurious β^+ contributions. Because that strength is at low energy, it is strongly weighted by β-decay phase space. The strongly weighted spurious strength might help to explain some of our negative forbidden decay contributions. While we feel it important to note these issues, Fig. 13 suggests that their impact is limited. Indeed, first-forbidden decay contributes about 14% of the total decay rate on average in this mass region. If we remove the four largest contributions (^{89}Ge and the three Zn isotopes—notable outliers), first-forbidden decays contribute less than 10% to the total rate on average. The spurious contributions in a few nuclei are interesting, then, but not critical.

IV. CONSEQUENCES FOR THE *R* PROCESS

In rare-earth nuclei, our calculation produces rates that are either consistently larger than or smaller than (depending on the functional) those of, e.g., Ref. [17]. We now use these new rates in simulations of the r process. The resulting rare-earth abundances are shown in Fig. 14. Generally, calculations that predict low rates build up the rare-earth peak in both hot and cold r-process trajectories, and calculations that predict higher rates (SLy5 and UNEDF1-HFB) reduce the peak. Our neutron star merger calculation (bottom panel of Fig. 14) demonstrates a different effect: Longer-lived nuclei broaden the rare-earth peak, and shorter-lived nuclei narrow it. For all three trajectories the change in abundances is fairly localized, with the effects caused by our most reliable parametrizations (SkO′, SkO′-Nd, and SV-min) modifying abundances by factors, roughly, of two to four.

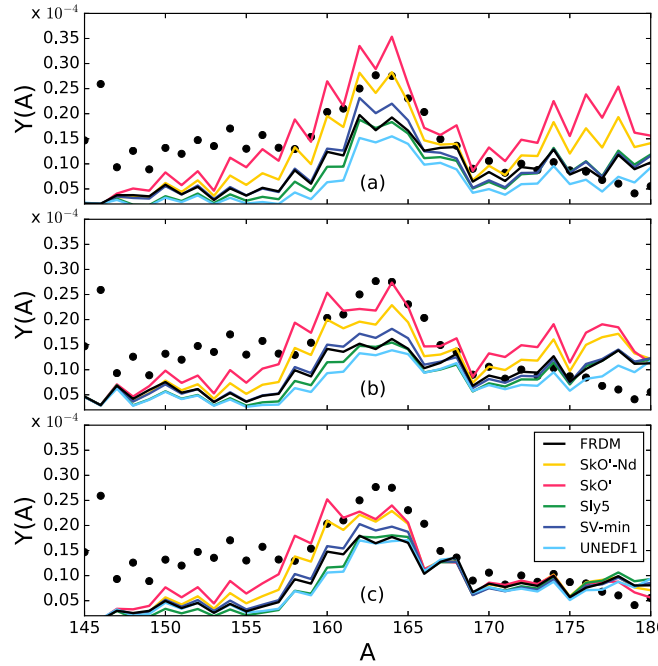

FIG. 14. The effect of our new β-decay rates on final r-process abundances. The same trajectories are used as in Fig. 2: (a) hot, (b) cold, and (c) nsm. Black circles mark solar abundances.

Near $A = 80$, our calculations produce small changes in weak r-process abundances from those obtained with the β-decay rates of Ref. [17] and larger changes from those with compilations. Figure 15 shows the baseline weak r-process calculation from the sensitivity study of Fig. 3 (blue line), where the β-decay lifetimes are taken from the REACLIB database [86][4] everywhere. We compare this abundance pattern to those produced when the β-decay rates for the set of 45 nuclei calculated in this work are replaced with our rates (red), those of Ref. [17] (purple), and those from Ref. [45] (teal). Although the differences in abundance produced by our rates and those of Ref. [17] are fairly small, differences produced by ours and those of Ref. [45] or REACLIB are noticeable, with the widely used REACLIB rates producing the most divergent results. It appears that many β-decay rates near $A = 80$ in the REACLIB database come from a much older QRPA calculation [87] that differs significantly from the

[4] https://groups.nscl.msu.edu/jina/reaclib/db/

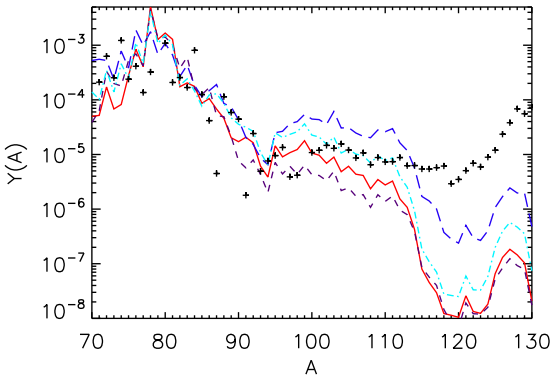

FIG. 15. Impact of our β-decay rates near $A = 80$ on weak r-process abundances, with rates from this work (red solid line), Ref. [17] (purple short dashes), Ref. [45] (light blue dot dashes), and the REACLIB database [86] (dark blue long dashes). Black crosses mark solar abundances.

more modern calculations, especially in lighter nuclei. In some instances, our rates differ from those listed in REACLIB by a factor of seven.

Even though many of our calculated rates are higher than those of Ref. [17] (Fig. 12), their impact on a weak r-process abundance pattern is not a uniform speeding-up of the passage of material through this region, as appears to be the case for a main r process (see, e.g., Ref. [7]). β-decay rates can influence how much neutron capture occurs in the $A \sim 80$ peak region and, consequently, how many neutrons remain for capture elsewhere [9]. Higher rates do not necessarily lead to a more robust weak r process; in fact, the opposite is more usually the case, because more capture in the peak region generally leads to fewer neutrons available for capture above the peak. This effect is illustrated in Fig. 16, which compares the abundance pattern for the baseline weak r-process simulation from Sec. III A with those obtained by using subsets of our newly calculated rates in the same simulation. Consider first the influence of the rates of the iron isotopes (green line in Fig. 16), particularly ^{76}Fe. This $N = 50$ closed shell nucleus lies on the r-process path, below the $N = 50$ nucleus closest to stability along the path ^{78}Ni. Thus an increase to the β-decay rate of ^{76}Fe over the baseline causes more material to move through the iron isotopic chain and reach the long waiting point at ^{78}Ni. The abundances near the $A \sim 80$ peak increase and those above the peak region decrease because the neutrons used to shift material from the very abundant ^{76}Fe to ^{78}Ni are no longer available for capture elsewhere. Changes to the β-decay rates of nuclei just above the $N = 50$ closed shell, however, can have a quite different effect on the pattern. The germanium isotopes, particularly ^{86}Ge and ^{88}Ge, are just above the $N = 50$ closed shell, so increases to their β-decay rates from the baseline will move material out of those isotopes to higher A (orange line in Fig. 16). Thus, abundances above the peak increase and more material makes it to the next closed shell, $N = 82$. In the end, the two very different effects partly cancel one another so that our rates do not change abundances significantly compared to those obtained with the rates of Ref. [17].

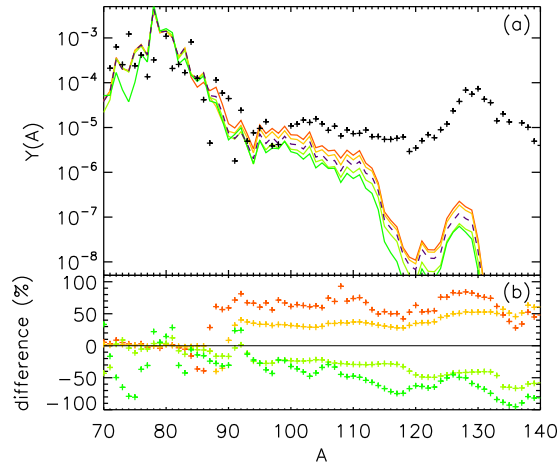

FIG. 16. (a) Abundance pattern for the baseline trajectory described in the text, using the rates of Ref. [17] rates for all of the key nuclei identified in Sec. II (black dashed line), compared to results of simulations with the same astrophysical trajectory and with new rates for $^{68-72}$Cr only (light green line), new rates for $^{72-76}$Fe only (green line), new rates for $^{86-92}$Ge only (yellow line), and new rates for $^{89-95}$As only (orange line). (b) Percent difference between the abundances produced by the baseline simulation (black line) and the simulations with the new rates (colored lines).

Given that modern QRPA calculations appear to have converged to roughly a factor of two or so, we use Monte Carlo variations to investigate the influence of this amount of uncertainty in all the β-decay rates required for r-process simulations. We start with astrophysical trajectories that seem typical for three types of main r-process environments (hot wind, cold wind, and merger). Then, for each Monte Carlo step, we vary all of the β-decay rates by factors sampled from a log-normal probability distribution,

$$p(x) = \frac{1}{x\sqrt{2\pi}\sigma} \exp\left[-\frac{(\mu - \ln(x))^2}{2\sigma^2}\right], \qquad (42)$$

where μ is the mean, and σ is the standard deviation of the underlying normal distribution and x is a random variable. We take $\mu = 0$ and $\sigma = \ln(1.4)$ which yields a spread in random rate factors corresponding roughly to the factor of two uncertainty in modern QRPA calculations (see, e.g., Ref. [33]). For each set of rate factors generated with the log-normal distribution the r-process simulation is then rerun. Figure 17 shows the resulting final r-process abundance pattern variances for 10 000 such steps. In each case, though some abundance pattern features stand out as clear matches or mismatches to the solar pattern, the widths of the main peaks and the size and shape of the rare-earth peak are not clearly defined. The real uncertainty in β-decay rates is larger than a factor of two because all QRPA calculations miss what could be important low-lying correlations. Thus, more work is needed, whether it be theoretical refinement or advances in experimental reach.

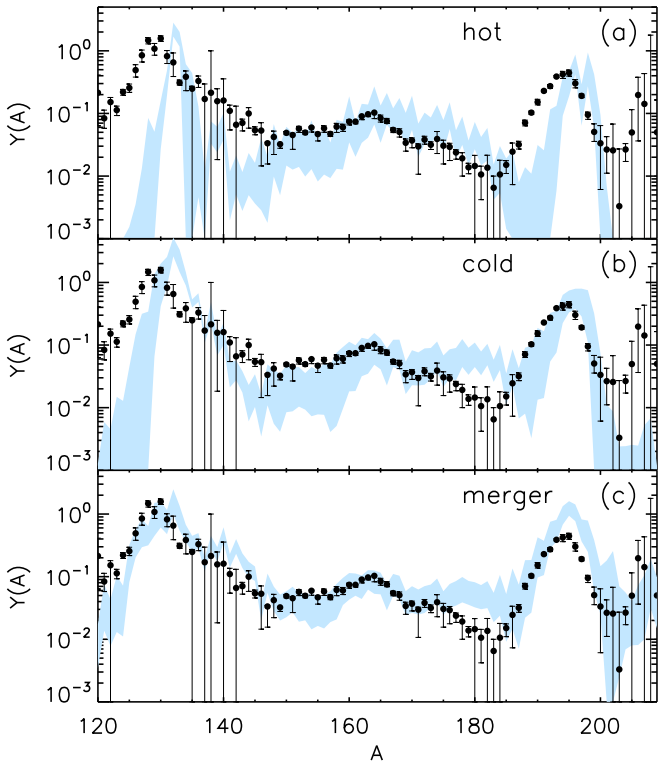

FIG. 17. Ranges of abundance patterns produced from Monte Carlo sampling of all β-decay lifetimes assuming roughly a factor of two rate uncertainty from a log-normal distribution in three main r-process trajectories: hot (a), cold (b), and merger (c) as in Ref. [88]. Points are solar residuals from Ref. [2].

V. CONCLUSIONS

We have adapted the proton-neutron finite-amplitude method (pnFAM) to calculate the linear response of odd-A and odd-odd nuclei, as well as the even-even nuclei for which it was originally developed, by extending the method to the equal-filling approximation (EFA). The fast pnFAM can now be used to compute strength functions and β-decay rates in all nuclei.

After optimizing the nuclear interaction to best represent half-lives in each mass region separately, we have calculated new half-lives for 70 rare-earth nuclei and 45 nuclei near $A = 80$. Our calculated half-lives are broadly similar to those obtained in the global calculations of Möller *et al.* [17] as well as to those of more recent work. As a result, r-process abundances derived from our calculated half-lives are similar to those computed with the standard rates of Ref. [17]. Our calculations support the conclusions of Ref. [33], which compared multiple QRPA β-decay calculations and found that they all had similar predictions. Still, the comparison of r-process predictions with much older ones in the REACLIB database and the discussion of uncertainty in Sec. IV demonstrate the need for continued work on nuclear β decay.

ACKNOWLEDGMENTS

T.S. gratefully acknowledges many helpful conversations with M. T. Mustonen, clarifying notes on SV-min from P.-G. Reinhardt, a useful HFB fitting program from N. Schunck, and discussions with D. L. Fang. This work was supported by the US Department of Energy through the Topical Collaboration in Nuclear Science "Neutrinos and Nucleosynthesis in Hot and Dense Matter," under Contract No. DE-SC0004142; through Early Career Award Grant No. SC0010263 (C.F.); and under individual Contracts No. DE-FG02-97ER41019 (J.E.), No. DE-FG02-02ER41216 (G.C.M.), and No. DE-SC0013039 (R.S.). M.M. was supported by the National Science Foundation through the Joint Institute for Nuclear Astrophysics Grants No. PHY0822648 and No. PHY1419765 and under the auspices of the National Nuclear Security Administration of the US Department of Energy at Los Alamos National Laboratory under Contract No. DE-AC52-06NA25396. We carried out some of our calculations in the Extreme Science and Engineering Discovery Environment (XSEDE) [89], which is supported by National Science Foundation Grant No. ACI-1053575, and with HPC resources provided by the Texas Advanced Computing Center (TACC) at The University of Texas at Austin.

APPENDIX: RESTORING ANGULAR MOMENTUM SYMMETRY

Deformed intrinsic states like those we generate in HFBTHO require angular-momentum projection. Here we use the rotor model [90,91], which is equivalent to projection in the limit of many nucleons or rigid deformation [34]. Even-even nuclei, with $K = 0$ ground states (K is the intrinsic z component of the angular momentum) are particularly simple rotors. Their "laboratory-frame" reduced matrix elements are just proportional to full intrinsic ones [91],

$$\langle J\ K||\hat{O}_J||0\,0\rangle = \Theta_K \langle K|\hat{O}_{JK}|0\rangle_{\rm intr}, \tag{A1}$$

where $\Theta_K = 1$ for $K = 0$ and $\Theta_K = \sqrt{2}$ for $K > 0$. The corresponding transition strength to an excited state $|J\ K\rangle$ is

$$B(\hat{O}_J;\, 0\,0 \to J\ K) = \Theta_K^2 |\langle K|\hat{O}_{JK}|0\rangle_{\rm intr}|^2. \tag{A2}$$

FAM strength functions are essentially composed of squared matrix elements [29,85], so we simply multiply $K > 0$ strength functions by $\Theta_K^2 = 2$.

The situation is more complicated in odd nuclei, which $K \neq 0$ ground-state angular momenta. The transformation between laboratory and intrinsic frames, corresponding to Eq. (A1), includes an additional term involving the time-reversed intrinsic state $|\overline{K_i}\rangle$ [91]:

$$\begin{aligned}\langle J_f\ K_f||\hat{O}_\lambda||J_i\ K_i\rangle = \sqrt{2J_i+1}[&(J_i\ K_i;\lambda\ K_i - K_f|J_f\ K_f)\\ &\times\langle K_f|\hat{O}_{\lambda,K_f-K_i}|K_i\rangle_{\rm intr}\\ &+(J_i - K_i;\lambda\ K_i + K_f|J_f\ K_f)\\ &\times\langle K_f|\hat{O}_{\lambda,K_f+K_i}|\overline{K_i}\rangle_{\rm intr}].\end{aligned} \tag{A3}$$

If we neglect rotational energies in comparison with intrinsic energies, we can sum over J_i that appear in Eq. (A3) to

obtain [90]

$$B(\hat{O}_\lambda;\, J_i\, K_i \to K_f) = \frac{1}{2J_i+1}\sum_{J_f=|J_i-\lambda|}^{J_i+\lambda} |\langle J_f\, K_f||\hat{O}_\lambda||J_i\, K_i\rangle|^2 = |\langle K_f|\hat{O}_{\lambda,K_i-K_f}|K_i\rangle_{\rm intr}|^2 + |\langle K_f|\hat{O}_{\lambda,K_i+K_f}|\overline{K_i}\rangle_{\rm intr}|^2. \quad \text{(A4)}$$

The EFA pnFAM, by preserving time-reversal symmetry and providing the combined transition strength from auxiliary states $\alpha^\dagger_\Lambda|\Phi\rangle$ and $\alpha^\dagger_{\bar{\Lambda}}|\Phi\rangle$, directly yields the terms in Eq. (A4). For example, the Gamow-Teller decay of a nucleus with $J_i = K_i = 3/2$ involves, according to Eq. (A4), three intrinsic transitions:

$$\left\langle\tfrac{3}{2}\middle|\hat{O}_{K=0}\middle|\tfrac{3}{2}\right\rangle,\quad \left\langle\tfrac{5}{2}\middle|\hat{O}_{K=1}\middle|\tfrac{3}{2}\right\rangle,\quad \left\langle\tfrac{1}{2}\middle|\hat{O}_{K=-1}\middle|\tfrac{3}{2}\right\rangle.$$

The third matrix element is equivalent because of time-reversal symmetry to $\langle-\frac{1}{2}|\hat{O}_{K=1}|-\frac{3}{2}\rangle$, up to a phase. Thus, a half-life calculation to each band requires a $K = 0$ transition and a pair of $K = 1$ transitions from states $|\frac{3}{2}\rangle$ and $|-\frac{3}{2}\rangle$. These are the auxiliary states that make up the EFA-pnFAM strength function. As a result, we obtain the total strength to a band in an odd nucleus the same way as in an even one: $S_{\rm total}(F;\omega) = S_{K=0}(F;\omega) + 2S_{K=1}(F;\omega)$ for Gamow-Teller transitions. The calculation of forbidden strength is similar. The factor of two for $K > 0$ strength cancels the factors of $1/2$ that appear in the EFA strength function in Eq. (33). $K = 0$ transitions do not need this factor because, e.g., $K = 3/2 \to K = 3/2$ and $K = -3/2 \to K = -3/2$ transitions are equivalent and come together in the strength function.

[1] E. M. Burbidge, G. R. Burbidge, W. A. Fowler, and F. Hoyle, Rev. Mod. Phys. **29**, 547 (1957).
[2] M. Arnould, S. Goriely, and K. Takahashi, Phys. Rep. **450**, 97 (2007).
[3] S. Shibagaki, T. Kajino, G. J. Mathews, S. Chiba, S. Nishimura, and G. Lorusso, ApJ **816**, 79 (2016).
[4] M. Mumpower, R. Surman, G. McLaughlin, and A. Aprahamian, Prog. Part. Nucl. Phys. **86**, 86 (2016).
[5] M. Mumpower, J. Cass, G. Passucci, R. Surman, and A. Aprahamian, AIP Advances **4**, 041009 (2014).
[6] P. Möller, J. Nix, and K.-L. Kratz, At. Data Nucl. Data Tables **66**, 131 (1997).
[7] J. Engel, M. Bender, J. Dobaczewski, W. Nazarewicz, and R. Surman, Phys. Rev. C **60**, 014302 (1999).
[8] O. L. Caballero, A. Arcones, I. N. Borzov, K. Langanke, and G. Martinez-Pinedo, arXiv:1405.0210.
[9] M. Madurga, R. Surman, I. N. Borzov, R. Grzywacz, K. P. Rykaczewski, C. J. Gross, D. Miller, D. W. Stracener, J. C. Batchelder, N. T. Brewer, L. Cartegni, J. H. Hamilton, J. K. Hwang, S. H. Liu, S. V. Ilyushkin, C. Jost, M. Karny, A. Korgul, W. Królas, A. Kuźniak, C. Mazzocchi, A. J. Mendez, K. Miernik, S. W. Padgett, S. V. Paulauskas, A. V. Ramayya, J. A. Winger, M. Wolińska-Cichocka, and E. F. Zganjar, Phys. Rev. Lett. **109**, 112501 (2012).
[10] P. T. Hosmer, H. Schatz, A. Aprahamian, O. Arndt, R. R. Clement, A. Estrade, K.-L. Kratz, S. N. Liddick, P. F. Mantica, W. F. Mueller, F. Montes, A. C. Morton, M. Ouellette, E. Pellegrini, B. Pfeiffer, P. Reeder, P. Santi, M. Steiner, A. Stolz, B. E. Tomlin, W. B. Walters, and A. Wöhr, Phys. Rev. Lett. **94**, 112501 (2005).
[11] P. Hosmer, H. Schatz, A. Aprahamian, O. Arndt, R. R. C. Clement, A. Estrade, K. Farouqi, K.-L. Kratz, S. N. Liddick, A. F. Lisetskiy, P. F. Mantica, P. Möller, W. F. Mueller, F. Montes, A. C. Morton, M. Ouellette, E. Pellegrini, J. Pereira, B. Pfeiffer, P. Reeder, P. Santi, M. Steiner, A. Stolz, B. E. Tomlin, W. B. Walters, and A. Wöhr, Phys. Rev. C **82**, 025806 (2010).
[12] C. Mazzocchi, R. Surman, R. Grzywacz, J. C. Batchelder, C. R. Bingham, D. Fong, J. H. Hamilton, J. K. Hwang, M. Karny, W. Królas, S. N. Liddick, P. F. Mantica, A. C. Morton, W. F. Mueller, K. P. Rykaczewski, M. Steiner, A. Stolz, J. A. Winger, and I. N. Borzov, Phys. Rev. C **88**, 064320 (2013).
[13] K. Miernik, K. P. Rykaczewski, R. Grzywacz, C. J. Gross, D. W. Stracener, J. C. Batchelder, N. T. Brewer, L. Cartegni, A. Fijałkowska, J. H. Hamilton, J. K. Hwang, S. V. Ilyushkin, C. Jost, M. Karny, A. Korgul, W. Królas, S. H. Liu, M. Madurga, C. Mazzocchi, A. J. Mendez, D. Miller, S. W. Padgett, S. V. Paulauskas, A. V. Ramayya, R. Surman, J. A. Winger, M. Wolińska-Cichocka, and E. F. Zganjar, Phys. Rev. C **88**, 014309 (2013).
[14] K. Takahashi and M. Yamada, Prog. Theor. Phys. **41**, 1470 (1969).
[15] S. Koyama, K. Takahashi, and M. Yamada, Prog. Theor. Phys. **44**, 663 (1970).
[16] K. Takahashi, Prog. Theor. Phys. **45**, 1466 (1971).
[17] P. Möller, B. Pfeiffer, and K.-L. Kratz, Phys. Rev. C **67**, 055802 (2003).
[18] M. T. Mustonen, T. Shafer, Z. Zenginerler, and J. Engel, Phys. Rev. C **90**, 024308 (2014).
[19] S. Perez-Martin and L. M. Robledo, Phys. Rev. C **78**, 014304 (2008).
[20] R. Surman, J. Engel, J. R. Bennett, and B. S. Meyer, Phys. Rev. Lett. **79**, 1809 (1997).
[21] M. R. Mumpower, G. C. McLaughlin, and R. Surman, Phys. Rev. C **85**, 045801 (2012).
[22] M. R. Mumpower, G. C. McLaughlin, and R. Surman, Astrophys. J. **752**, 117 (2012).
[23] M. R. Mumpower, G. C. McLaughlin, R. Surman, and A. W. Steiner, arXiv:1603.02600.
[24] C. Fröhlich, G. Martínez-Pinedo, M. Liebendörfer, F.-K. Thielemann, E. Bravo, W. R. Hix, K. Langanke, and N. T. Zinner, Phys. Rev. Lett. **96**, 142502 (2006).
[25] J. Pruet, R. D. Hoffman, S. E. Woosley, H.-T. Janka, and R. Buras, Astrophys. J. **644**, 1028 (2006).
[26] S. Wanajo, Astrophys. J. **647**, 1323 (2006).
[27] F.-K. Thielemann, A. Arcones, R. Käppeli, M. Liebendörfer, T. Rauscher, C. Winteler, C. Fröhlich, I. Dillmann, T. Fischer, G. Martinez-Pinedo, K. Langanke, K. Farouqi, K.-L. Kratz, I. Panov, and I. K. Korneev, Prog. Part. Nucl. Phys. **66**, 346 (2011).

[28] A. Arcones and F. Montes, ApJ **731**, 5 (2011).
[29] T. Nakatsukasa, T. Inakura, and K. Yabana, Phys. Rev. C **76**, 024318 (2007).
[30] P. Avogadro and T. Nakatsukasa, Phys. Rev. C **84**, 014314 (2011).
[31] M. Kortelainen, N. Hinohara, and W. Nazarewicz, Phys. Rev. C **92**, 051302 (2015).
[32] T. Nikšić, N. Kralj, T. Tutiš, D. Vretenar, and P. Ring, Phys. Rev. C **88**, 044327 (2013).
[33] M. T. Mustonen and J. Engel, Phys. Rev. C **93**, 014304 (2016).
[34] P. Ring and P. Schuck, *The Nuclear Many-Body Problem (Theoretical and Mathematical Physics)* (Springer, New York, 2005).
[35] J.-P. Blaizot and G. Ripka, *Quantum Theory of Finite Systems* (The MIT Press, Cambridge, 1985).
[36] M. Stoitsov, N. Schunck, M. Kortelainen, N. Michel, H. Nam, E. Olsen, J. Sarich, and S. Wild, Comput. Phys. Commun. **184**, 1592 (2013).
[37] N. Schunck, J. Dobaczewski, J. McDonnell, J. Moré, W. Nazarewicz, J. Sarich, and M. V. Stoitsov, Phys. Rev. C **81**, 024316 (2010).
[38] S. Perez-Martin and L. M. Robledo, Phys. Rev. C **76**, 064314 (2007).
[39] A. L. Goodman, Nucl. Phys. **352**, 30 (1981).
[40] H. Sommermann, Ann. Phys. **151**, 163 (1983).
[41] D. Vautherin and N. Mau, Nucl. Phys. **422**, 140 (1984).
[42] P. Ring, L. Robledo, J. Egido, and M. Faber, Nucl. Phys. **419**, 261 (1984).
[43] F. Alasia, O. Civitarese, and M. Reboiro, Phys. Rev. C **39**, 1012 (1989).
[44] J. L. Egido and P. Ring, J. Phys. G: Nucl. Part. Phys. **19**, 1 (1993).
[45] T. Marketin, L. Huther, and G. Martínez-Pinedo, Phys. Rev. C **93**, 025805 (2016).
[46] I. Borzov, S. Fayans, and E. Trykov, Nucl. Phys. **584**, 335 (1995).
[47] J. Krumlinde and P. Möller, Nucl. Phys. **417**, 419 (1984).
[48] M. R. Mumpower, G. C. McLaughlin, and R. Surman, Phys. Rev. C **86**, 035803 (2012).
[49] R. Surman, M. Mumpower, R. Sinclair, K. L. Jones, W. R. Hix, and G. C. McLaughlin, AIP Advances **4**, 041008 (2014).
[50] B. S. Meyer, Phys. Rev. Lett. **89**, 231101 (2002).
[51] I. V. Panov and H.-T. Janka, Astron. Astrophys. **494**, 829 (2009).
[52] S. Goriely, A. Bauswein, and H.-T. Janka, Astrophysical Journal Letters **738**, L32 (2011).
[53] R. Surman, G. C. McLaughlin, M. Ruffert, H.-T. Janka, and W. R. Hix, ApJ **679**, L117 (2008).
[54] S. Wanajo, Y. Sekiguchi, N. Nishimura, K. Kiuchi, K. Kyutoku, and M. Shibata, ApJ **789**, L39 (2014).
[55] Z. Y. Xu, S. Nishimura, G. Lorusso, F. Browne, P. Doornenbal, G. Gey, H.-S. Jung, Z. Li, M. Niikura, P.-A. Söderström, T. Sumikama, J. Taprogge, Z. Vajta, H. Watanabe, J. Wu, A. Yagi, K. Yoshinaga, H. Baba, S. Franchoo, T. Isobe, P. R. John, I. Kojouharov, S. Kubono, N. Kurz, I. Matea, K. Matsui, D. Mengoni, P. Morfouace, D. R. Napoli, F. Naqvi, H. Nishibata, A. Odahara, E. Şahin, H. Sakurai, H. Schaffner, I. G. Stefan, D. Suzuki, R. Taniuchi, and V. Werner, Phys. Rev. Lett. **113**, 032505 (2014).
[56] J. Dobaczewski and J. Dudek, Acta Phys. Pol. B **27** (1996).
[57] M. Bender, P.-H. Heenen, and P.-G. Reinhard, Rev. Mod. Phys. **75**, 121 (2003).
[58] E. Perlińska, S. G. Rohoziński, J. Dobaczewski, and W. Nazarewicz, Phys. Rev. C **69**, 014316 (2004).
[59] M. Bender, J. Dobaczewski, J. Engel, and W. Nazarewicz, Phys. Rev. C **65**, 054322 (2002).
[60] P.-G. Reinhard, D. J. Dean, W. Nazarewicz, J. Dobaczewski, J. A. Maruhn, and M. R. Strayer, Phys. Rev. C **60**, 014316 (1999).
[61] P. Klüpfel, P.-G. Reinhard, T. J. Bürvenich, and J. A. Maruhn, Phys. Rev. C **79**, 034310 (2009).
[62] J. D. McDonnell (private communication).
[63] E. Chabanat, P. Bonche, P. Haensel, J. Meyer, and R. Schaeffer, Nucl. Phys. **635**, 231 (1998).
[64] M. Kortelainen, J. McDonnell, W. Nazarewicz, P.-G. Reinhard, J. Sarich, N. Schunck, M. V. Stoitsov, and S. M. Wild, Phys. Rev. C **85**, 024304 (2012).
[65] S. Fracasso and G. Colò, Phys. Rev. C **76**, 044307 (2007).
[66] M. Kortelainen, T. Lesinski, J. Moré, W. Nazarewicz, J. Sarich, N. Schunck, M. V. Stoitsov, and S. Wild, Phys. Rev. C **82**, 024313 (2010).
[67] M. Kortelainen, J. McDonnell, W. Nazarewicz, E. Olsen, P.-G. Reinhard, J. Sarich, N. Schunck, S. M. Wild, D. Davesne, J. Erler, and A. Pastore, Phys. Rev. C **89**, 054314 (2014).
[68] K. Bennaceur and J. Dobaczewski, Comput. Phys. Commun. **168**, 96 (2005).
[69] J. Dobaczewski, W. Nazarewicz, and T. R. Werner, Phys. Scr. **T56**, 15 (1995).
[70] W. Satuła, J. Dobaczewski, and W. Nazarewicz, Phys. Rev. Lett. **81**, 3599 (1998).
[71] G. Audi, M. Wang, A. Wapstra, F. Kondev, M. MacCormick, X. Xu, and B. Pfeiffer, Chin. Phys. C **36**, 1287 (2012).
[72] M. Wang, G. Audi, A. Wapstra, F. Kondev, M. MacCormick, X. Xu, and B. Pfeiffer, Chin. Phys. C **36**, 1603 (2012).
[73] G. Audi and A. Wapstra, Nucl. Phys. **595**, 409 (1995).
[74] G. Audi, F. Kondev, M. Wang, B. Pfeiffer, X. Sun, J. Blachot, and M. MacCormick, Chin. Phys. C **36**, 1157 (2012).
[75] H. Akimune, I. Daito, Y. Fujita, M. Fujiwara, M. B. Greenfield, M. N. Harakeh, T. Inomata, J. Jänecke, K. Katori, S. Nakayama, H. Sakai, Y. Sakemi, M. Tanaka, and M. Yosoi, Phys. Rev. C **52**, 604 (1995).
[76] C. J. Guess, T. Adachi, H. Akimune, A. Algora, S. M. Austin, D. Bazin, B. A. Brown, C. Caesar, J. M. Deaven, H. Ejiri, E. Estevez, D. Fang, A. Faessler, D. Frekers, H. Fujita, Y. Fujita, M. Fujiwara, G. F. Grinyer, M. N. Harakeh, K. Hatanaka, C. Herlitzius, K. Hirota, G. W. Hitt, D. Ishikawa, H. Matsubara, R. Meharchand, F. Molina, H. Okamura, H. J. Ong, G. Perdikakis, V. Rodin, B. Rubio, Y. Shimbara, G. Süsoy, T. Suzuki, A. Tamii, J. H. Thies, C. Tur, N. Verhanovitz, M. Yosoi, J. Yurkon, R. G. T. Zegers, and J. Zenihiro, Phys. Rev. C **83**, 064318 (2011).
[77] J. K. Tuli, Nuclear Wallet Cards, National Nuclear Data Center (Brookhaven National Laboratory, Upton, accessed August 11, 2014).
[78] J.-L. Basdevant, J. Rich, and M. Spiro, *Fundamentals in Nuclear Physics: From Nuclear Structure to Cosmology (Advanced Texts in Physics S)* (Springer, New York, 2005).
[79] P. Sarriguren, Phys. Rev. C **91**, 044304 (2015).
[80] T. Munson, J. Sarich, S. M. Wild, S. Benson, and L. Curfman McInnes, *TAO 3.6 Users Manual*, Technical Memorandum ANL/MCS-TM-322 (Argonne National Laboratory, Argonne, 2015).

[81] C. Gaarde, J. Larsen, M. Harakeh, S. van der Werf, M. Igarashi, and A. Müller-Arnke, Nucl. Phys. **334**, 248 (1980).
[82] Evaluated Nuclear Structure Data File, April 16, 2014, [http://www.nndc.bnl.gov/ensarchivals/].
[83] D.-L. Fang, Phys. Rev. C **93**, 034306 (2016).
[84] I. N. Borzov, Phys. Rev. C **67**, 025802 (2003).
[85] N. Hinohara, M. Kortelainen, and W. Nazarewicz, Phys. Rev. C **87**, 064309 (2013).
[86] R. H. Cyburt, A. M. Amthor, R. Ferguson, Z. Meisel, K. Smith, S. Warren, A. Heger, R. D. Hoffman, T. Rauscher, A. Sakharuk, H. Schatz, F. K. Thielemann, and M. Wiescher, Astrophys. J. Suppl. Ser. **189**, 240 (2010).
[87] H. Klapdor, J. Metzinger, and T. Oda, At. Data Nucl. Data Tables **31**, 81 (1984).
[88] R. Surman, M. Mumpower, J. Cass, I. Bentley, A. Aprahamian, and G. C. McLaughlin, EPJ Web Conferences **66**, 07024 (2014).
[89] J. Towns, T. Cockerill, M. Dahan, I. Foster, K. Gaither, A. Grimshaw, V. Hazlewood, S. Lathrop, D. Lifka, G. D. Peterson, R. Roskies, J. R. Scott, and N. Wilkens-Diehr, Comp. Sci. Engineering **16**, 62 (2014).
[90] A. Bohr and B. R. Mottelson, *Nuclear Structure* (World Scientific, Singapore, 1998).
[91] A. Bohr and B. R. Mottelson, *Nuclear Structure, Volume II: Nuclear Deformations* (W. A. Benjamin, New York, 1975).